CHAPTER 6

EPR OF MONONUCLEAR NON-HEME IRON PROTEINS

Betty J. Gaffney
Department of Biological Science, Florida State University

Flexible geometry of three- to six-protein side-chain ligands to non-heme iron in proteins is the basis for widely diverse reactivites ranging from iron transport to redox chemistry. The gap between fixed states determined by x-ray analysis can be filled by spectroscopic study of trapped intermediates. EPR is a versatile and relatively quick approach to defining intermediate states in terms of the geometry and electronic structures of iron. A number of examples in which the iron chemistry of non-heme proteins is understood through x-ray structures at subbond length resolution, refined calculations, and spectroscopy exist now. Some examples in which EPR has provided unique insight are summarized in Table 1. Assignment and quantitative evaluation of the EPR resonances in ferric, non-heme iron sites is the focus of the first section of this review. An earlier chapter in this series provides more background on the theory specific to EPR of $S = 5/2$ metal ions [1]. Besides EPR spectra of ferric mononuclear sites, EPR of ferrous iron coupled to a spin 1/2 radical, as it pertains to the categories mononuclear and non-heme, will also be covered, in the second half of this chapter. Examples include the quinone–ferrous interactions in photosynthetic reaction centers and nitric oxide complexes with non-heme ferrous iron. Other recent reviews of the biochemistry and spectroscopy of non-heme iron proteins provide additional background [2–6].

1. EPR OF MONONUCLEAR, HIGH-SPIN FERRIC NON-HEME PROTEINS

1.1. Assignment: The $S = 5/2$ EPR Parameter Space Is Large but Not Infinite

Two accidentally similar EPR spectra provide a focus for discussion of assigning transitions in high-spin, non-heme ferric proteins. Several superoxide reductase (SOR) enzymes have been characterized recently [7]. The SOR from *Pyrococcus furiosus* has an EPR spectrum, shown in Figure 1 [8], superficially resembling that

G. Hanson, L. Berliner (eds.), *High Resolution EPR*, Biological Magnetic Resonance 28,
DOI 10.1007/978-0-387-84856-3_6,

Table 1. References for Representative High-Spin Ferric Proteins Characterized by EPR, X-Ray Structure, and Calculation

Protein	EPR analysis	x-ray structure	Calculation
Phenylalanine hydroxylase	13, 6	67	69
Lipoxygenase	14	68	70
Transferrin	13	11	none

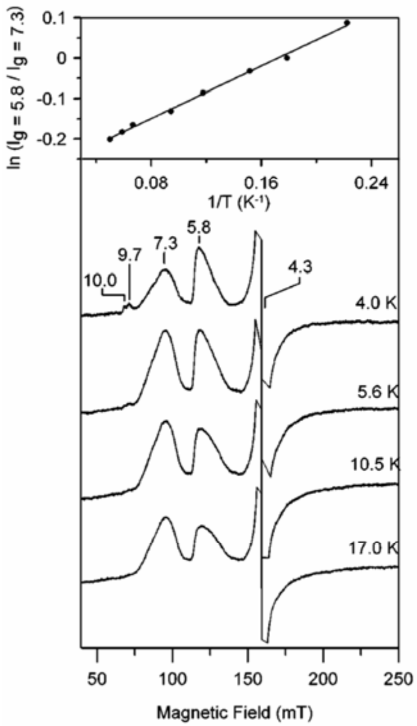

Figure 1. EPR spectra of ferric iron in superoxide reductase (SOR) of *Pyrococcus furiosus*. X-band EPR spectra, at low temperature (as indicated on the figure), of recombinant SOR (0.5 mM) in 50 mM HEPES, pH 7.5, are shown. The ratio of intensities at $g = 5.8$ (middle Kramers doublet) and $g = 7.3$ (lower Kramers doublet) is shown in the upper panel. The figure is from Fig. 2 of Clay et al. [8], with permission of the publisher.

of the oxalate complex of ferric transferrin, shown in Figure 2 [9]. Iron ligands in SOR are four histidines, the thiolate of a cysteine, and either a carboxylate or water [10]. In contrast, the sidechains ligating iron in transferrin are two Tyr, one His, and one Asp. The remaining transferrin iron ligands are provided by bidentate coordination of an anion [9,11]. Diferric transferrin, with high-spin iron bound in both lobes, has a variety of EPR spectra depending on the associated anion and

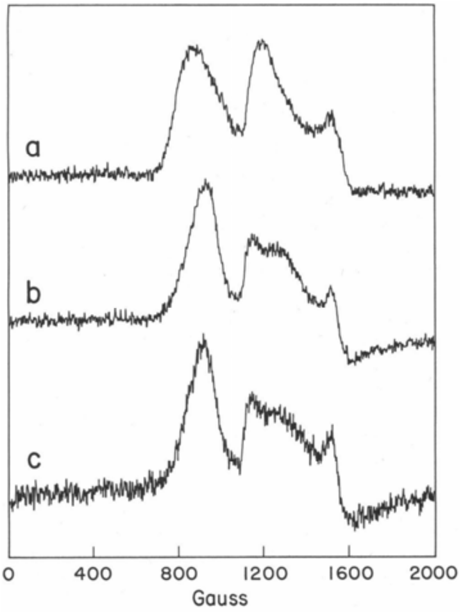

Figure 2. EPR spectra of transferrin samples in 0.09 M HEPES, pH 7.5, diluted with 2 M NaCl to final NaCl concentrations of 0 M (a), 0.5 M (b), and 1.0 M (c), and final protein concentrations of 1.0, 0.75, and 0.5 mM transferrin in a, b, and c, respectively. The figure is reproduced from Fig. 5 of Dubach et al. [9], with permission of the publisher.

ionic conditions of the buffer. It is the oxalate complex that has an EPR spectrum most similar to the SOR spectrum. The resonances shown in the examples of Figures 1 and 2 cover *g*-values greater than 4, although the full spectra extend to *g*-values of 2.0 or less. The low-field regions of X-band EPR spectra provide the basis for assigning values of the zero-field splitting (zfs) terms *E* and *D* in spectra of numerous non-heme, high-spin ferric proteins. Low-field regions of the EPR spectra are much more diverse for ferric non-heme proteins than for the heme counterparts, but as will be illustrated, there is more to assigning the spectra than the *g*-values of the resonances. Assignment of features in EPR spectra of high-spin iron proteins is the first step in quantitative assessment of the number and nature of the species present.

Non-heme iron proteins frequently require reconstitution with iron after they are isolated. Reconstitution of *P. furiosus* SOR yields samples with iron in two kinds of site, each with a unique EPR spectrum. Determining which EPR spectrum corresponds to the catalytically active iron site required correlation of an increase in one with increases in enzyme activity. In addition, assignment of one of the EPR resonances to the redox active iron component was made by quantitative comparison of ferric signals obtained at points through a dye-mediated redox titration [8]. In a similar problem regarding reconstituted phenylalanine hydroxylase (PAH), one ferric site, among several sites contributing to the EPR spectrum, had to be assigned to active site iron [12]. A model including a distribution in the zero-field splitting parameter E/D was adopted to make the quantitative comparison of the two EPR spectra arising from reconstituted PAH ([13] and references therein). Ferric lipoxygenase also has two overlapping EPR spectra, the ratio of which is sensitive to buffer conditions. Both components of lipoxygenase EPR spectra are from active enzyme. Again, spectra were fit according to a distribution in the central E/D value for each site, and the amount of each component was then determined [14]. In the diferric transferrins, assignment of resonances and computer fitting of EPR spectra were used to compare spectra of the carbonate complex to those of complexes with other anions, such as oxalate [9,13].

The following discussion covers approaches to accurate and quantitative assignment of EPR spectra and the role of the experimental variables, temperature, and multiple EPR frequencies in making the assignments. As will be seen, the two ferric subjects of Figures 1 and 2 differ in the sign and magnitude of the zero-field splitting parameter D.

1.2. Assignment for Zero-Field Splitting: the Zeeman Term

The spin Hamiltonian Eq. (1) has well-known solutions when the microwave frequency is less than the zero-field splitting D (at X-band, $\nu \sim 9.4$ GHz or $\nu/c \sim 0.3\ \mathrm{cm}^{-1}$). The six energy levels for $S = 5/2$ arrange in three Kramers doublets at zero field and, for D large compared with $h\nu$, diverge linearly with magnetic field until the fields are larger than usually used for X-band spectroscopy:

$$\begin{aligned} H_\mathrm{S} &= g\beta_e H_0 \cdot \mathbf{S} + \mathbf{S} \cdot \mathbf{D} \cdot \mathbf{S} \\ &= g\beta_e H_0 \cdot \mathbf{S} + D(S_z^2 - S(S+1)/3) + E(S_x^2 - S_y^2) \\ &\quad + \text{terms fourth order in } \mathbf{S} \text{ (minor for most proteins samples).} \end{aligned} \tag{1}$$

Figure 3 summarizes how the g-values of the transitions vary with orientation of principal magnetic axes in the magnetic field and with the zero-field terms D (positive) and E. The numbers shown at selected points on the figure are transition probabilities. The bold numbers (e.g., 5 to 6) signify the order of the six energy levels; 6 is highest in energy. Some notable features in Figure 3 are that cases with E/D of zero or ~1/3 yield simple spectra because only one transition has significant probability. A transition at $g = 6.0$ dominates the spectrum when E/D is 0 (axial), and alternatively a transition at $g = 4.3$ dominates when E/D is 1/3 (rhombic). Note also that the absorption at lowest field (highest g-value) corresponds to different principal directions of the D tensor for different transitions. The transition probabilities for the highest-energy-level pair (levels 5 to 6) are small, and absorptions arising from transitions between these levels are usually significant only when symmetry is near rhombic. The specification of principal axis directions to x, y, or z (see Fig. 3) results from choice of a coordinate system for the traceless $\mathbf{D}$ matrix such that $|D_z| \geq |D_y| \geq |D_x|$ and $1/3 \geq E/D \geq 0$ [1].

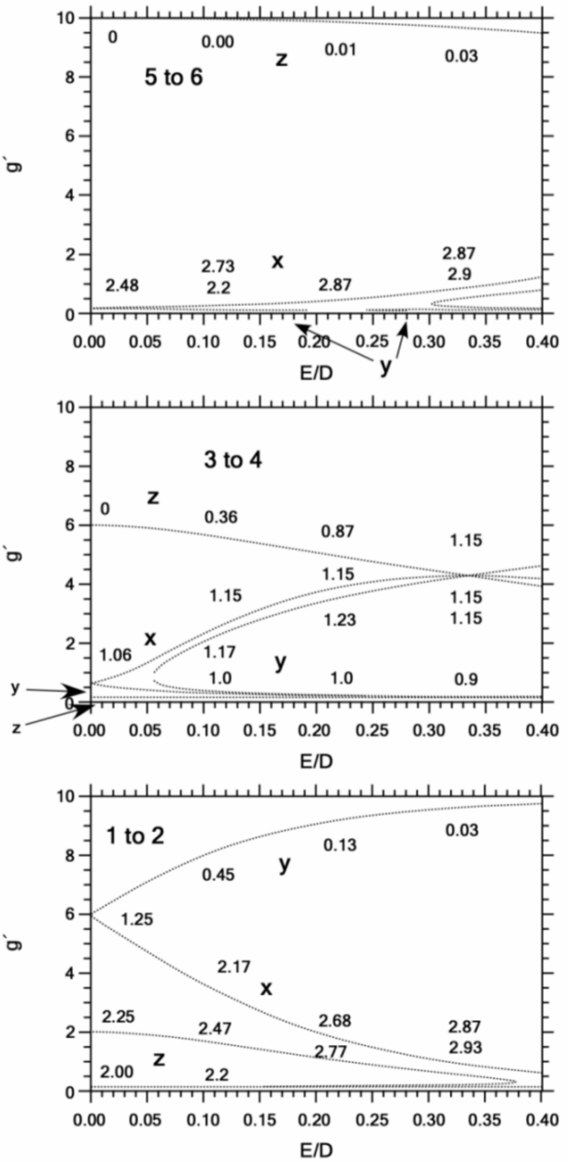

Figure 3. Calculated *g*-values for the full range of *E*/*D*. Calculations were performed with a value of $D = 2.0\ \mathrm{cm}^{-1}$ and X-band frequency. Transitions between pairs of energy levels are numbered in bold on each panel (1 to 2, etc.). The *g*-values along molecular *x*, *y*, and *z* principal axes are shown by dotted lines, and representative squared transition moments are given along those lines. The figure is reproduced from Fig. 9 of Gaffney and Silverstone [1], with permission of the publisher.

For *D* negative, the shape of the plot shown in the top panel of Figure 3 will replace the shape of the one at the bottom and vice versa: the shape of the bottom plot replaces that of the top. This switch has practical consequences in that temperature variation can be used to determine the order of the energy levels, and hence the sign of *D*, for symmetries yielding significant absorption from two doublets.

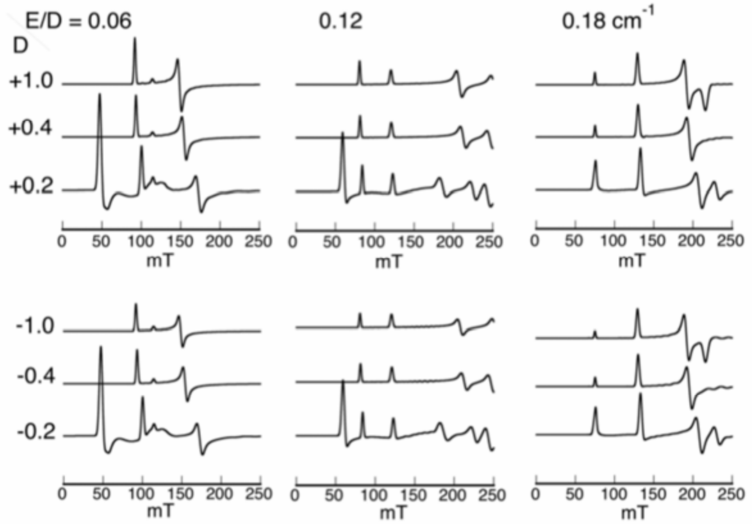

Figure 4. The low-field portions of calculated X-band EPR spectra of $S = 5/2$ for various values of *D* and *E/D*. Small changes in intensity differentiate spectra for positive (upper) and negative (lower) values of *D*. Spectra were calculated (with XSophe [37]) with frequency = 9.4 GHz, temperature = 15 K, linewidth = 140 MHz (Gaussian), magnetic field segments = 5 mT, and 32 angular grid partitions. The amplitudes of the spectra are adjusted to represent equivalent numbers of spins. The spectra have additional resonances at fields higher than those shown, but these are rarely observed experimentally because of broadening by distributions in *E* and *D*.

Metal centers of intermediate symmetry, with *E*/*D* in the range ~0.05–0.30, give rise to significant EPR transitions within more than one doublet. The pairing of *g*-values (see Fig. 3) permits assignment of the spectrum to one iron electronic state with multiple transitions rather than to single transitions from multiple states of iron in the same sample. For example, with $E/D = 0.06$, transition between levels 1 and 2 (for *D* positive and $>h\nu$) gives principal low-field g_y- and g_x-values of 7.3 and 4.5, and the low-field g_z-value for the 3 to 4 transition is ~5.9. Figure 4 shows calculated X-band EPR spectra for the range of *E*/*D* values from 0.06 to 0.18 to illustrate changes in the low-field features. The values of *D* are positive in the upper panel and negative in the lower one. The values of *D* used in the calculations are also varied from ±1.0 cm^{-1} (top row) and ±0.4 cm^{-1} (middle row) to ±0.2

cm^{-1} (lower row), illustrating the shifts in *g*-values that occur as *D* becomes significantly smaller than the X-band frequency, 0.3 cm^{-1}. Note also that a new resonance is evident at low field in the lower row of each panel, left and middle spectra. This new resonance, an interdoublet transition, arises from a transition in levels 2 and 3 when the difference in energy of two Kramers doublets (between 2*D* and 3*D* at zero field) is smaller than the microwave energy applied. Interdoublet transitions will be discussed in more detail in §1.3.

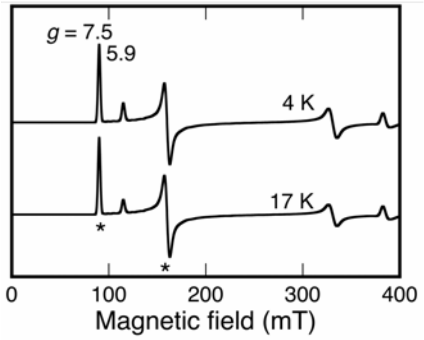

Figure 5. Variation with temperature of the relative intensities in a high-spin ferric EPR signal (*D* negative). The resonances from transitions in the lowest doublet are marked with stars. The resonance at $g = 5.9$ arises from the 3→4 transition. Increasing temperature increases the ratio of resonance at $g = 7.5$ to that at $g = 5.9$. The overall intensities of the spectra at the two temperatures are adjusted so that the first resonance is of the same amplitude in the two spectra. Additional resonances occur at higher fields than the region shown. The spectra were calculated (with XSophe [37]) with microwave frequency = 9.4 GHz, $D = -0.5$ cm^{-1}, $E/D = 0.07$, linewidth = 140 MHz, 60 magnetic field segments (0.6 T scan), and 32 angular partitions.

The temperature dependence of the ratio of overlapping EPR resonances provides information about the value of *D*. The spectra in Figure 5 are calculated for $D = -0.5$, $E/D = 0.07$, at two temperatures. The lowest doublet is marked by stars, and the middle doublet contributes the resonance at $g = 5.9$. The ratio of absorption at $g = 5.9$ divided by that at 7.5 *increases* with increasing temperature when *D* is *positive*. *D negative* gives a ratio of these resonances that *decreases* as temperature increases. The dependence on temperature of the relative intensities of two transitions depends on the Boltzmann population factors Eq. (2) for the *n* energy levels involved:

$$\left[e^{-E_n(B)/kT}\right] / \sum_{i=1}^{6} e^{-E_i(B)/kT} \ . \tag{2}$$

When the energies are small relative to *kT*, series expansions of the exponentials give the approximation Eq. (3) for the temperature dependence of relative intensities, I_k/I_l, of resonances arising from the separate pairs of levels, k and l, contributing to the spectrum

$$\ln(I_k / I_l) \propto 1/T\,. \tag{3}$$

The intensities in Eq. (3) are those of transitions within different doublets, so the slope of a plot of $\ln(I_k/I_l)$ against $(1/T)$ gives the sign and value of D. This approach was taken, for example, in assignment of a negative sign, and a magnitude near $|0.5|$ cm^{-1}, to the D-value of the iron center in oxidized SOR [8]. The two resonances at lowest field (g-values 7.5 and 5.9) are most convenient to use in application of Eq. (3) because they are less subject to broadening by distribution in E/D than the higher field resonances (refer to Fig. 4).

1.3. Assignment for Zero-Field Splitting Similar to the Zeeman Term

Many non-heme iron proteins have zero-field splitting energy similar to that of the Zeeman term when X-band EPR is measured. The angular variation of resonant fields and transition probabilities become interestingly nonlinear for these cases in which two terms are dominant, Zeeman (field dependent) and zero-field splitting (field independent), in the spin Hamiltonian. The EPR spectrum is being measured under conditions where all six levels of the $S = 5/2$ spin are close in energy, so significant contributions to the spectrum are possible from many of the 15 possible transitions between the six energy levels. The experimental sample transferrin oxalate has a D-value of ~+0.27 cm^{-1} and provides a good illustration (see Fig. 2). Choosing the magnetic field at one pair of angles, θ and ϕ, with respect to the molecular axes, produces the calculated energies and separations of energies shown in Figure 6. In the lower plot of separation of energies, the resonant fields for this molecular orientation are found from a horizontal line drawn at the applied microwave frequency. At X-band frequency, more than five different transitions from this single molecular orientation arise, as indicated by the line drawn on the figure. The usual Kramers doublet transitions are between levels 1 and 2, 3 and 4, and 5 and 6. The interdoublet transitions $2 \rightarrow 3$ and $4 \rightarrow 5$ also contribute significantly to resonances in the magnetic field range 0–400 mT. A characteristic of interdoublet transitions is that the separations of energy levels are curved for a wide range of θ and ϕ. The full angular variation of resonant fields for the $2 \rightarrow 3$ transition ($D = +0.27$ cm^{-1} and $E/D = 0.06$) is illustrated by a three-dimensional plot in Figure 7. In this figure the direction of the applied magnetic field relative to the molecular x, y, and z axes is signified by expression of the resonant magnetic field for each orientation in the B_x, B_y, and B_z space. A single octant is shown in the figure, but the pattern is symmetric and would appear as a dumbbell surface in four octants. One can immediately see from this figure why this interdoublet transition is called a "looping transition."

An instructive view of how transitions from all molecular orientations contribute to the observed EPR spectrum appears in a plot (Fig. 8) showing magnetic field

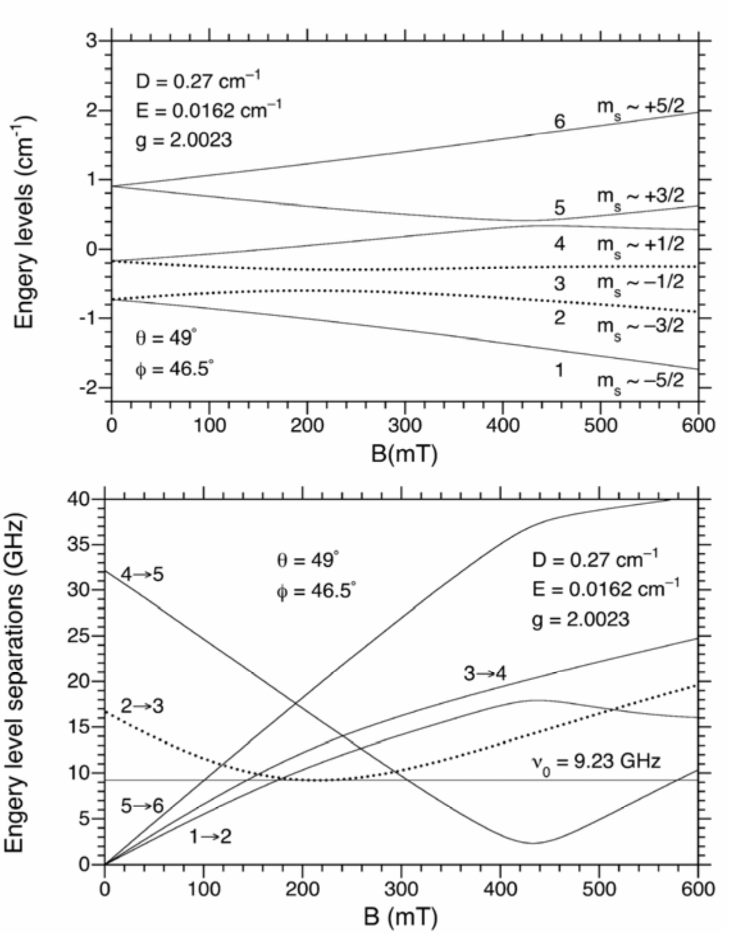

Figure 6. Energy levels and energy separations at selected molecular orientations. The energies calculated are part of simulations of transferrin oxalate EPR spectra. The molecular axes are oriented with respect to the magnetic field at (θ,ϕ) = (49°,46.5°). Transition between levels 2 and 3 is highlighted by dotted lines. Levels are numbered as in Figure 3, and parameters of the calculation are given on the figure. The horizontal line in the lower panel is drawn at an X-band frequency of 9.23 GHz. The figure is reproduced from Fig. 5 of Gaffney and Silverstone [21], with permission of the publisher.

variation in the intensity factor Eq. (4) for all θ and ϕ, for a transition between initial and final levels, *i* and *f*:

$$\text{Intensity factor} = \ |< i \,|\, S_{\perp} \,|\, f >|^{2}\ \sin\theta\,. \qquad (4)$$

Examination of this type of plot reveals that regions with a high density of transitions and a high intensity factor would dominate the associated EPR spectrum.

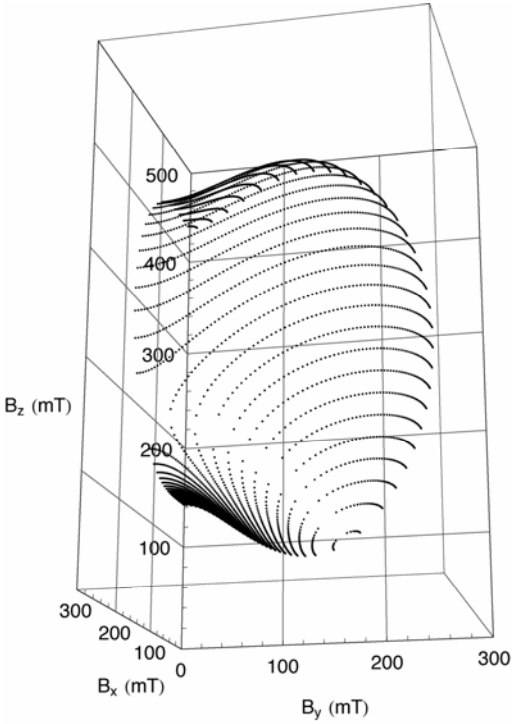

Figure 7. Three-dimensional representation of one octant of a looping transition. The resonant magnetic field for each angular orientation is plotted in magnetic field-space, where each vector from the origin to a point is graphed according to the *x*, *y*, and *z* components. Calculation parameters are the same as in Figure 6. The figure is reproduced from Fig. 7 of Gaffney and Silverstone [21], with permission of the publisher.

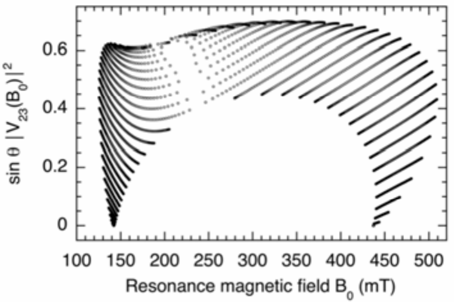

Figure 8. Intensity of resonances in a looping transition as a function of magnetic field. The intensity factor (*y*-axis) is shown for transitions between levels 2 and 3, using Eq. (4). Calculation parameters were $D = 0.27\ \text{cm}^{-1}$, $E = 0.0162\ \text{cm}^{-1}$, and microwave frequency = 9.23 GHz). The figure is reproduced from Fig. 11 of Gaffney and Silverstone [21], with permission of the publisher.

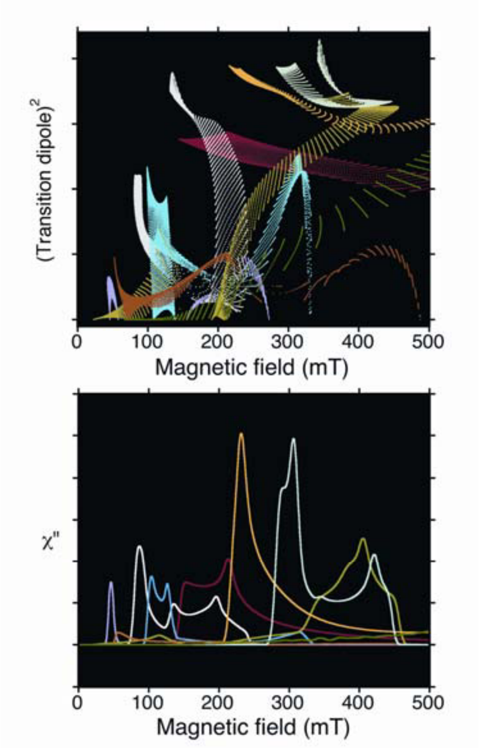

Figure 9. Intensity of all significant resonances for small *D*-value and X-band EPR. The upper figure shows the square of the transition dipole for each of the pairs of energy levels that contribute significantly to the low-field region of an X-band spectrum with small value of *D*. The lower figure shows the corresponding absorption spectra. The color code for transitions between pairs of energy levels is 1→2 (red), 1→3 (orange), 1→4 (pink), 2→3 (yellow), 2→4 (bright blue), 3→4 (turquoise), 3→5 (white), 4→5 (light green), and 5→6 (dark green). The input parameters for the IronHS program [1] were $D = 0.1$ cm^{-1}, $E/D = 0.06$, frequency = 9.4 GHz, linewidth = 140 MHz, field segments = 1 mT, steps in θ of 1°), and steps in ϕ of 2°. Regions of looping transitions were calculated using a cubic polynomial [21].

Some biomineral samples contain high-spin iron with values of $D < 0.2$, and the $S = 5/2$ spectra of some manganese centers in proteins have similarly small zero-field splittings. At X-band, for $D <$ ~0.2, most of the 15 possible transitions between pairs of energy levels become possible, and the spectra are a complex set of overlapping transitions. As an aid in assigning the EPR spectra of manganese lipoxygenase at X- and W-band frequencies, a plot of X-band intensity factors against magnetic field was examined for all of the significant transitions (9 of 15 possible in this case) with $S = 5/2$, $D = 0.1$ cm^{-1}, without the manganese hyperfine [15]. This set of parameters is equivalent to a high-spin ferric center with very small *D*. Figure 9, in which the intensity factors (upper figure) are colored differently for each transition, illustrates the calculation. The corresponding absorption spectra are given in the lower figure. The red points are for the well-behaved 1→2 transition, and the spectrum of this transition would have low-field maxima at points where the density of points is high, at about 140 and 210 mT. The other transitions shown also give intensity within the same magnetic-field region and, in the case of transitions 2→3 (yellow), 2→4 (bright blue), 3→4 (turquoise), and 3→5 (white), have high density of points and high enough intensity factors that they would add to the 1→2 transition in contributing to the spectrum. This figure readily explains why assignment of X-band EPR spectra of some ferric or manganous proteins with small D-value is daunting.

1.4. High-Frequency EPR and Assignment for Zero-Field Splitting: The Zeeman Term

In the previous sections, quantitative evaluation of the amount of ferric iron contributing to an EPR spectrum was referenced to the partial spectrum in the low-field region. This process is somewhat analogous to estimating the extent of an iceberg from the portion visible above water. The complexity of multiple overlapping transitions illustrated in Figures 6–9 can be avoided by choice of a different microwave frequency such that either $h\nu >$ or $h\nu < D$. For $h\nu > D$, high-frequency EPR at numerous frequencies is now available [16,17]. When the Zeeman term is dominant in Eq. (1) ($h\nu > D$), the energy levels of $S = 5/2$ are close to a nested set of doublets, diverging linearly with field except for the very-low-field region. Five transitions between the six levels occur (1→2, 2→3, 3→4, 4→5, and 5→6), and these are centered near $g = 2$. EPR spectra at 94 GHz (W-band) of diferric transferrin carbonate show this simplification (Fig. 10, experimental (a) and calculated (b)) [18]. The simulation illustrates the broadening of selected transitions (dotted lines above and below the calculated spectrum) that would result from a distribution in E and D. Comparing the experimental and calculated spectra reveals extra, low-intensity features on each side of the central region in the experimental spectrum that arise from a second component. Two components in the transferrin X-band EPR spectra are resolved in the low-field region [13]. The parameters from earlier assignments of transferrin X-band spectra [13] were chosen for the simulation of the W-band spectrum shown in Figure 10.

An experimental spectrum of manganese lipoxygenase, measured at 94 GHz [15], is shown in Figure 11 to illustrate the simplification achieved at higher frequency for an $S = 5/2$ sample with a D value ~0.07 cm^{-1}. Because this spectrum was recorded under saturating conditions, it has the appearance of an absorption spectrum, and the manganese hyperfine is overmodulated, so the spectrum is almost identical to that expected for high-spin ferric with the same value of D. A simulated spectrum is shown in the Figure 11 lower panel. A strong central resonance from transition in levels 3 and 4 dominates the spectrum. The outer wings of the spectrum arise from transitions in levels 1 and 2 and 5 and 6. Closer to the center of the spectrum, transitions in levels 2 and 3 and 4 and 5 contribute. The slightly more pronounced features on the low-field side of the spectrum than on the higher-field side are consistent with a positive D-value.

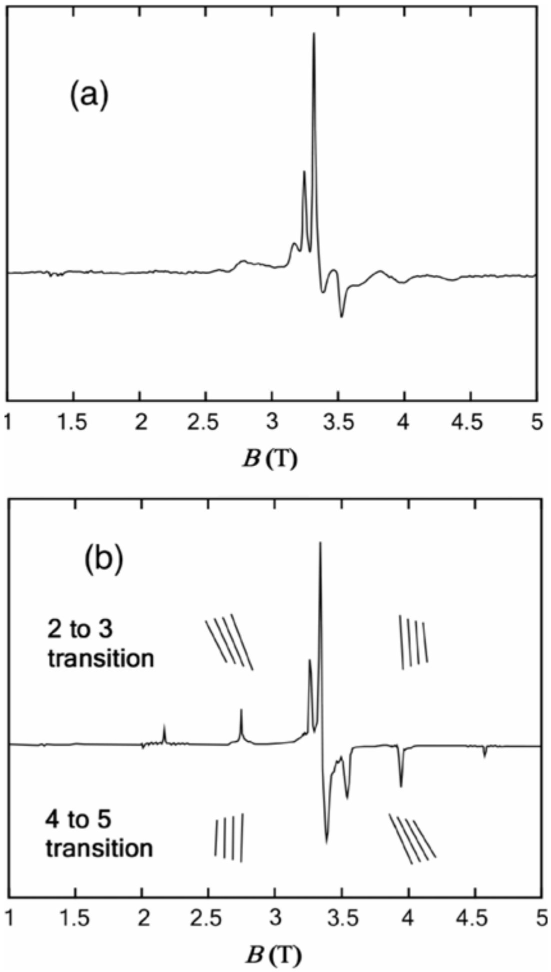

Figure 10. Experimental and calculated spectra of diferric transferrin carbonate at 94 GHz. Transferrin was ~1.5 mM in pH 7.4 buffer/salt solution with 50% glycerol. The experimental spectrum recorded at 40 K is shown in (a), and the conditions under which it was recorded were frequency = 94.090 GHz, modulation = 1.0 mT amplitude at 100 kHz, microwave power = 1 microW, and sampling rate = 8192 points/2T and 0.328 s/point. The spectrum shown in (b) was calculated (40 K) with the IronHS program [1] and the following parameters: frequency = 94.1 GHz, $D = 0.28\ \text{cm}^{-1}$, $E/D = 0.333$, width of Gaussian distribution in $E/D = 0.087$, linewidth = 150 MHz. Points are also shown above and below the calculated spectrum to illustrate how the magnetic-field positions of features for the interdoublet transitions between levels 2 and 3 and levels 4 and 5 would vary throughout a distribution in D (horizontal shifts) or E (vertical shifts). Similar width contributions would also apply to the outer transitions between levels 1 and 2 and 5 and 6. The figures are reproduced from Figs. 3 and 5 of Gaffney et al. [18], with permission of the publisher.

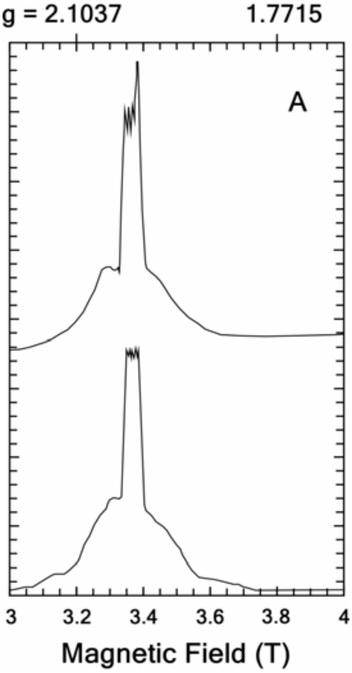

Figure 11. Manganese lipoxygenase 94 GHz experimental EPR spectrum and calculation. Manganese lipoxygenase was 0.5 mM in a pH 7.3 buffer with 28% glycerol. The experimental spectrum (upper) was recorded at 20 K and 94.094 GHz, with field modulation = 100 kHz, 1.0 mT amplitude; microwave power = 15.8 μW; time constant = 0.082 s; scan rate = 2 T/0.373 h, 8192 points. The spectrum is the average of one scan each of increasing and decreasing field. The calculated (XSophe [37]) absorption spectrum (lower) used D and E = 0.08 and 0.015 cm^{-1}, respectively, manganese hyperfine = 0.0086 cm^{-1}, linewidth = 84 MHz, and microwave frequency = 94.22 GHz. The figure is reproduced from Fig. 7a of Gaffney et al. [15], with permission of the publisher.

1.5. Contributions to Line Shapes

1.5.1. The "Aasa-Vänngård Factor"

In 1975, Aasa and Vänngård [19] pointed out that correct integrals of EPR spectra would be obtained from *frequency-swept* spectra, but because in EPR the magnetic field is usually swept, the spin-packet linewidth in field-swept EPR requires additional consideration. The linewidth has proper units of frequency (MHz), and the integral of the lineshape function with respect to frequency is normalized to one. The frequency to field change of variables is given by Eq. (5), where ν_0 is the microwave frequency and $\nu(B_0)$ is the frequency separation of the two levels involved in the transition at magnetic field B_0 [20,21]:

$$f(\sigma_\nu,(\nu(B)-\nu_0)) = f(\sigma_\nu,(B-B_0)\frac{d\nu(B_0)}{dB_0}+\frac{1}{2}(B-B_0)^2\frac{d^2\nu(B_0)}{dB_0^2}+...)\,. \tag{5}$$

Under conditions (low magnetic field, $D > h\nu$) giving energy levels diverging linearly with field, the practical result of Eq. (5) is that the field-swept linewidth is proportional to the frequency-swept linewidth divided by the effective g-factor:

$$\sigma_{\text{field}} \propto \frac{h\sigma_{\text{frequency}}}{g_{\text{eff}}\beta}\,. \tag{6}$$

Although g_{eff} is used in Eq. (6) to distinguish it from the electron g-factor, the remaining discussion will be phrased in terms simply of g, as is common in EPR. The increasing apparent linewidth with decreasing g-value in a field-swept EPR spectrum is apparent, for example, in the calculated spectra of Figure 5. Simulation of lineshapes provides the best approach to quantitative spin counts in field-swept EPR of ferric iron. Another approach to determining spin concentration in samples with wide EPR spectra is comparison to the double integral of a standard covering a similar magnetic-field range [12].

1.5.2. Relaxation

From a historical perspective, the insight provided by Aasa and Vänngård probably was not noticed in earlier EPR experiments with high-spin iron because heme proteins provided the subjects of many early biological EPR experiments. A characteristic of ferric heme EPR spectra is that the apparent field-swept linewidths at $g \sim 6$ and $g \sim 2$ do not vary as implied by Eq. (6). Instead, the apparent linewidths have significant relaxation-determined contributions [22,23] that vary across the spectrum. Relaxation times of high-spin iron in proteins, heme or non-heme, are of obvious importance for contemporary experiments designed to determine distances by EPR of iron-containing proteins [24–26]. For example, in a biological example involving a non-heme iron to spin-label distance measurement, an estimate of 23–30 Å between a hinge region in the ligand-gated channel, FepA, and the bound iron chelate, enterobactin, was obtained [27].

The relaxation times of enterobactin [27] can be compared with relaxation times of other biological non-heme, $S = 5/2$, iron examples, transferrin carbonate, and oxalate [28]. The observed EPR linewidths (>100 MHz) [13] of these non-heme iron proteins exhibit little temperature dependence (4–100 K), in contrast to observed widths of heme proteins. The measured phase memory times ($T_m \leq T_2$) of the transferrins correspond to relaxation-determined linewidth contributions of <2 MHz in the range 4–30 K. The T_m values of enterobactin bound to FepA indicate similarly small relaxation-determined widths. The apparent widths of these non-heme-iron EPR spectra therefore have an origin other than relaxation.

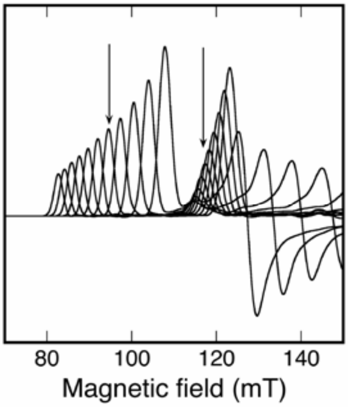

Figure 12. An ensemble of calculated EPR spectra related to distributions in *E/D* for $S = 5/2$. The low-field region of resonances for a constant value of D (–0.5 cm^{-1}) and variable E, at 4 K, is shown. The range of *E/D* is from 0.03 to 0.11. The arrows point to the g-values corresponding to *E/D* of 0.07, similar to those in the EPR spectrum of superoxide reductase [8]. In the figure, each spectrum is scaled to represent equivalent spins. In the case of a distribution in values of *E/D*, the amplitudes of the subspectra would be multiplied by an appropriate distribution function. Other calculation parameters (XSophe [37]) are microwave frequency = 9.6 GHz, magnetic field partitions = 0.5 mT, 64 angular grid partitions, and linewidth = 140 mT. The resonances in the magnetic field range 84~117 mT are the g_y features of transitions in the lowest doublet; only two of the g_x features from the same transition appear in the magnetic field region shown: they are the two resonances at the extreme right side of the figure. There are other resonances at higher magnetic fields than those shown.

1.5.3. Distributions in Zero-Field Splitting

Distributions in zero-field splittings are generally accepted as the dominant form broadening the apparent linewidths in EPR spectra of non-heme, high-spin iron proteins [13,14,22,29]. Because transition probabilities vary with *E*/*D* (Fig. 3), shapes arising from distributions are different from ones calculated with a single frequency-swept lineshape of width similar to experimentally observed ones. This point is illustrated in Figure 12. Each full subspectrum, only part of which is shown, has a double integral corresponding to the same number of spins (more transitions occur at fields higher than those shown).

The parameters chosen for Figure 12 give spectra that might be included, for example, in fitting the low-field lineshape of ferric superoxide reductase (Fig. 1), or (with some change in the value and sign of *D*) transferrin oxalate (Fig. 2), or the high-salt form of ferric lipoxygenase [14]. As the value of *E*/*D* decreases, the two sets of resonances shown in the figure move closer together, converging on $g = 6$ when *E*/*D* is zero. Fitting would involve applying a distribution model (Gaussian or multicomponent, for example) to adjust the amplitudes of the subspectra within the distribution. The lowest-field set of maxima (~84–117 mT) in Figure 12 covers a wider field range than the next set (~118–122 mT). As a result, a distribution of *E*/*D* would have the effect of diminishing the intensity of the lowest-field maximum in the spectrum relative to that of the second-to-lowest-field maximum. This consideration probably applies to the experimental SOR spectrum in Figure 1. On the other hand, the smaller *D*-value, as well as distribution of *E*/*D,* contributes to relative intensities in the transferrin oxalate spectra in Figure 2. Distributions in *D* might also contribute to breadth in EPR spectra of the types considered here.

1.5.4. Looping Transitions

Interesting cases for simulation arise when looping transitions occur, mentioned earlier in §1.3 and Figures 6–8 [20,21,30]. A looping transition occurs when a pair of energy levels is in resonance at two separate magnetic fields. For a "powder" EPR sample, a range of angular orientations may contribute looping transitions to the spectrum, whereas outside of that range no transitions occur between the same pair of levels (Fig. 7). When the two transitions of a looping transition are separated in a magnetic field by a few linewidths, special simulation methods are required to represent the spectrum accurately while minimizing the number of calculated field points and matrix diagonalizations. With reference to Eq. (5), as conditions (angular orientation) approach the point at which the two resonances overlap, and $d\nu(B_0)/dB_0$ goes to zero, a different approach to the lineshape function is required. One approach is to approximate $(\nu(B) - \nu_0)$ by a cubic polynomial in B, Eq. (7), where the constants c_0 and c_1 are defined in terms of the two resonant fields (B_{01} and B_{02}) and the derivatives $d\nu(B)/dB$ at points 1 and 2 [21]:

$$\nu(B) - \nu_0 \sim (B - B_{01})(B - B_{02})(c_0 + c_1 B) . \tag{7}$$

In essence, $h(\nu(B) - \nu_0)$ is the difference between the curved energy separation (for example, the 2→3 transition in Fig. 6) and the microwave energy, $h\nu_0$. The transition probability variation requires similar adjustment. Figure 13 illustrates the considerations for the selected angular orientation used in earlier figures (Figs. 6–8). In Figure 13a, the dots are the calculated separations of energy levels through the region of the loop; the straight lines are the slopes, $d\nu(B_0)/dB_0$, at the two resonant fields; the cubic fit is shown by the solid line; and the shaded area corresponds to a linewidth $\pm\sigma_\nu$ (150 MHz). Clearly, $d\nu(B_0)/dB_0$ is not constant over a linewidth. The standard approximation (two diagonalizations) would apply a shape function to the two points where the loop crosses $(\nu(B) - \nu_0) = 0$ and approximate $(\nu(B) - \nu_0)$ by $(B - B_0)$ in the normalized lineshape function. An exact calculation uses a frequency-swept function calculated at closely spaced intervals (many diagonalizations) through the looping region. These approaches can be compared to the "cubic approximation" in which $(\nu(B) - \nu_0)$ is approximated by Eq. (7), using just two points (Fig. 13b,c). The approximate calculation is the dashed line, and the dots are the overlap of exact calculation or cubic approximation.

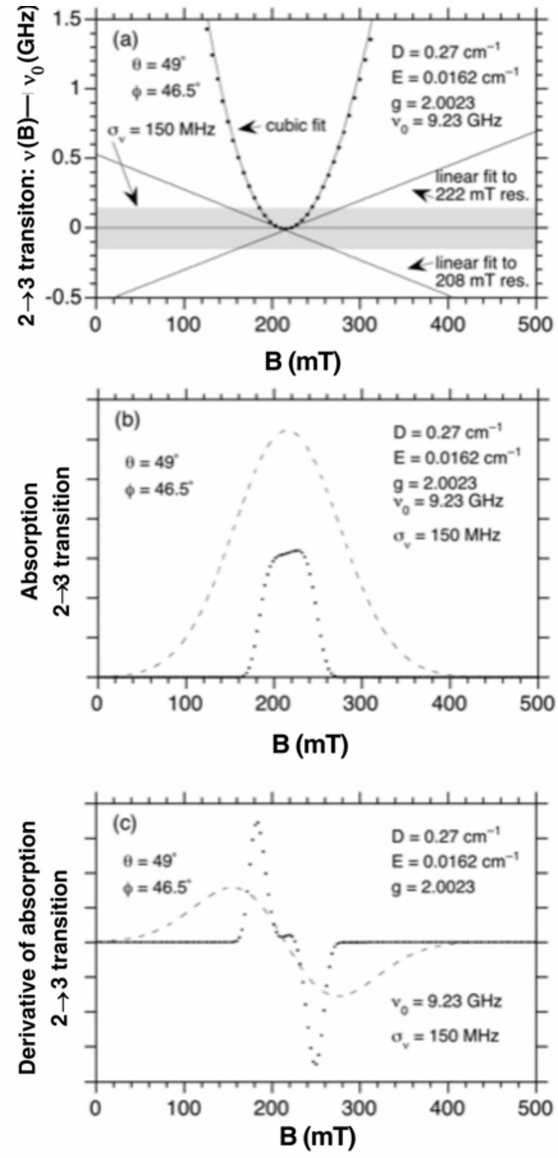

Figure 13. Simulation of a "looping" transition using linear and cubic fits. (a) Cubic fits (solid line) and calculated difference between the transition frequency and the microwave frequency (dots), compared with linear fits (straight lines) in the region of a looping transition. (b) Corresponding absorption spectra with (dashed line) and without (dotted line) the cubic approximation. (c) Derivative spectra. Calculation parameters are the same as in Figure 6. The figure is reproduced from Fig. 6 of Gaffney and Silverstone [21], with permission of the publisher.

2. EPR OF MONONUCLEAR, LOW-SPIN FERRIC NON-HEME PROTEINS

2.1. Nitrile Hydratase

Low-spin ferric iron is common in heme and in some iron–sulfur proteins, but nitrile hydratase is presently the lone example among mononuclear, non-heme, non-iron–sulfur iron proteins [31]. The ferric form of the enzyme is obtained by photolysis of the as-isolated nitric oxide d^6 form. The g-values of the photodissociated ferric protein are 2.27, 2.13, and 1.97, and photointermediates of differing g-values are observed. The relatively narrow linewidths allowed the ^{57}Fe hyperfine to be measured at g_z (40 MHz), establishing that the **g**- and iron **A**-tensors are 45° out of alignment.

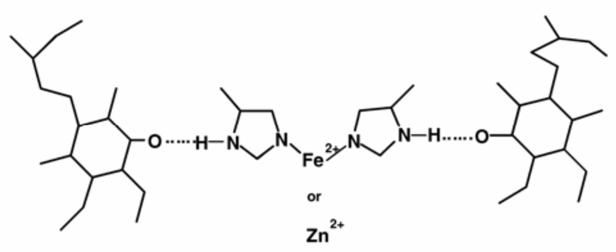

Scheme 1.

3. RADICAL ($S = 1/2$) PROBES OF FERROUS ($S = 2$) IRON

3.1. Photosynthetic Reaction Centers

Photosynthetic reaction centers are the classic example of ferrous iron: EPR invisible at 9 GHz because of large zero-field splitting, rendered visible by interaction with close radical spins. The nature of the path (~7–9 Å, Scheme 1) between iron and quinones A and B (Q_A and Q_B) is favorable for a spin–spin coupling to be the dominant form of interaction. Essentially, each level of the $S = 2$ system is split by the $S = 1/2$ spin, giving energy separations accessible at 9 GHz. The A or B quinone radical interactions with the metal ion can be probed separately by means of preparation light pulses and temperature cycles [32] or by selective extraction procedures [33]. Recent summaries are available of the history of assigning the complex Q–Fe spectra and selecting individual quinone interactions with iron [32,34]. Feher has written a personal and historical account of his experimental studies, extending from development of EPR spectrometers and the ENDOR technique to pathways of electron transfer in photosynthesis [35].

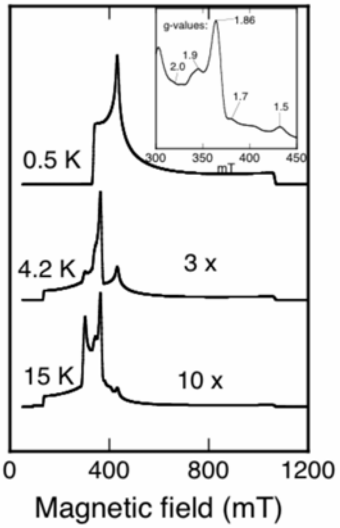

Figure 14. Calculated absorption EPR spectra of ferrous iron ($S = 2$) interacting by J-coupling with a radical at 8.7 Å. The temperatures in the calculations are 0.5, 4.2, and 15 K. The amplitudes of calculated spectra corresponding to equivalent spins were multiplied by the values given on the figure for display. The inset marks selected g-values in the 15 K spectrum. The 0.5 K spectrum is complete as shown, but the 15 K spectrum extends to near 1 T (not shown). The calculation parameters (XSophe [37]) are simplified (isotropic value of J) from those reported in [36] and [41]: iron g-values = 2.16, 2.27, and 2.04; $J = 0.4$ cm^{-1}; $D = 5.2$ cm^{-1}; and $E/D = 0.25$. Other calculation parameters include microwave frequency = 9.0 GHz and linewidth = 30 G (narrower than experimental). Spectra were calculated with 80 field partitions and 64 grid segments.

For purposes of discussing the EPR of iron–semiquinone interactions in reaction centers, simplified simulations of the spectra are given in Figure 14. The parameters chosen for the simulation are similar to those of Calvo et al. [36]. The spin Hamiltonian relevant to a one-electron reduced Q_A–Fe–Q_B system has terms involving the iron zero-field splitting and the semiquinone–iron electron spin–spin interactions:

$$H = (\text{iron Zeeman}) + (\text{quinone radical Zeeman}) + \mathbf{S} \cdot \mathbf{D} \cdot \mathbf{S} + \mathbf{S}_{\text{FeII}} \cdot \mathbf{J} \cdot \mathbf{S}_{\text{Q}}. \quad (8)$$

Zero-field splitting ($\mathbf{S} \cdot \mathbf{D} \cdot \mathbf{S}$) dominates the overall appearance of the spectrum for the Q–Fe case. In the absence of a radical, ferrous iron with $D = 5.2$ cm^{-1} would have no spectrum unless frequencies considerably higher than 9 GHz were used. The radical splits the iron energy levels through a spin–spin interaction. The relevant term, $\mathbf{S}_{\text{FeII}} \cdot \mathbf{J} \cdot \mathbf{S}_{\text{Q}}$, includes isotropic exchange and an anisotropic part that consists of both dipolar and exchange interaction components. The isotropic exchange component can be expressed as $J_0 \boldsymbol{S}_{\text{FeII}} \boldsymbol{S}_{\text{Q}}$. When the point dipole approximation is appropriate for one spin (semiquinone), the anisotropic interaction can be described by a vector connecting the spins and by two angles defining the orientation of the interspin vector in the magnetic axis frame of the other spin (ferrous iron, $S = 2$). Different conventions are used for the sign of J. The convention used in Eq. (8) is that of the XSophe simulation program [37], for which the input parameters for spin–spin interaction are J_0, r, χ, and ρ. Positive J_0 signifies antiferromagnetic spin–spin interaction in XSophe. The notation used by Feher and colleagues [36] is that negative J_0 signifies the antiferromagnetic spin–spin interaction.

Experimental conditions for observing semiquinone–iron interactions by EPR, at low temperature, favor absorption-like rapid-passage spectra. Calculated *absorption* spectra are shown in Figure 14 to illustrate major characteristics of EPR spectra of the $S = 2$, $S = 1/2$ interactions in Q–Fe centers. In the figure, the portion of the spectrum arising from the ground $S = 2$ doublet is illustrated in the calculation with temperature taken as 0.5 K. As the temperature is raised (4.2 and 15 K), more complex spectra that include transitions between higher pairs of levels are seen. The linewidth chosen for the illustration in Figure 14 is considerably less than the experimental linewidth, to show the details of the transitions. In experimental spectra, the overall signal is broad and has a maximum at $g' = \sim 1.8$ when the temperature is 1.4 K or higher [38,39]. Experimental samples also differ from the calculation in Figure 14 in having an intense $g = 2$ signal from several radicals.

The Figure 14 inset identifies g-values in the region where semiquinone–iron signals are often monitored. The positions of the g-values are sensitive to D, to E/D, and somewhat to J and are relatively insensitive to the iron–radical distance, r, in the relevant 7- to 9-Å range (the coordinates of Q_B vary in this range with sample conditions [40]). The two reaction-center quinones have very similar magnetic properties and distances to iron, so the approximate calculation shown in Figure 14 could apply to either Q–Fe interaction. In photosystem II (PSII) of the cyanobacterium *Thermosynechococcus elongatus*, a peak at a g-value of 1.97 is attributed to the Q_B semiquinone–iron interaction, and peaks at g-values in the 1.93–1.95 range to either radical–iron interaction [32]. In addition, the biradical state in which both Q_A and Q_B are semiquinones has a well-defined peak at a g-value of 1.66 in the *T. elongatus* photosystem sample. The biradical state is of course not spectroscopically equivalent to the monoradical state discussed so far.

Characterizing the semiquinone as a point dipole in simulations of Q–Fe EPR works well because the radical is a small perturbation on the highly anisotropic ferrous iron energy levels, but for a high-resolution understanding of why the electron interaction between reaction-center quinones is so efficient, a better picture of the electronic properties of each semiquinone is desired. The paramagnetism of iron is not necessary for electronic interaction between the quinones, and iron either can be driven to low-spin ($S = 0$) by cyanide addition or can be replaced by the diamagnetic metal Zn^{2+} in photosynthetic systems. Under these conditions, and with high-frequency EPR, the relative intensities of $Q_A^{-\bullet}$ and $Q_B^{-\bullet}$, as a function of the state of the sample, can be examined [33]. In addition, the exchange interaction of quinones in the biradical state ($Q_A^{-\bullet}Q_B^{-\bullet}$) of zinc-substituted reaction centers has been examined by relaxation and by high-frequency EPR [36,41].

3.2. Nitric Oxide and Non-Heme Ferrous Centers

Nitric oxide (NO) is used commonly by EPR spectroscopists as a tool to render ferrous iron measurable [42,43]. In oxidases, nitric oxide interacting with iron serves as a mimic of oxygen activation. Through advances in higher-frequency ENDOR, the intimate details of the structure of non-heme iron oxidase intermediates are being revealed by studies of Fe–NO complexes [44]. Interest is also increasing in the proteins involved in natural NO-dependent biological responses. Bacterial stress regulons are activated by agents including NO, reactive oxygen, and drugs in a variety of categories [45]. The NO-response regulons are involved in bacterial defense against macrophage attack, a process including NO generation by these animal cells. Crosstalk also occurs between genes regulated by iron levels and the NO regulons [46]. Progress in characterizing the non-heme iron–NO complexes of several transcription regulators will be mentioned below. These include Fur, a regulator of iron acquisition, and NorR, an NO-responsive transcription factor. Superoxide reductase (SOR), mentioned earlier in the ferric EPR sections, is an enzyme component of the stress response to superoxide. The SOR mononuclear Fe–NO complex has been a useful analog of the Fe-superoxide interaction in this enzyme. The reader is referred to the chapter on iron–sulfur proteins for further discussion of another category of NO additions to iron. The many examples of heme–iron proteins interacting with NO are also covered in Chapters 8 and 9.

Experimentally, nitric oxide complexes of iron proteins have excellent properties for sensitive spectroscopy. The EPR signals are strong enough that they can sometimes be measured within intact *Escherichia coli* expressing the target protein [47], and EPR signals can be observed at higher temperatures, sometimes including room temperature, than are normally required for study of other spin states of non-heme iron [48]. Among the factors contributing to the strong signals are large zero-field splitting (only the ground state is populated at lower temperatures), relatively small deviations from axial symmetry, small distributions in E/D (the short Fe–NO bond is a well-defined axial ligand), and of near-coincidence of the g- and hyperfine tensors. Some of these favorable properties contribute to the spectra in Figure 15, which shows the EPR spectra of the iron–nitric oxide complex of lipoxygenase at two frequencies, 9.26 and 92.6 GHz, scaled to the same g-value scale. The essentially identical g-values in the two spectra indicate that the D-value of this Fe–NO complex is >93 GHz (~3 cm^{-1}). These spectra show the presence of two species, the relative amounts of which vary with pH and other factors [49]. Variability of two components exhibited in spectroscopy of lipoxygenase is also a property of both the ferric and ferrous forms of the protein [14,50]. The apparent linewidth in the 92.6 GHz spectrum is narrower on the g-value scale shown than that in the 9.26 GHz spectrum, indicating that relaxation is probably a significant component of the linewidth, especially of the outer features in the spectrum. This spectrum is part of an ongoing investigation (Gaffney, *unpublished*).

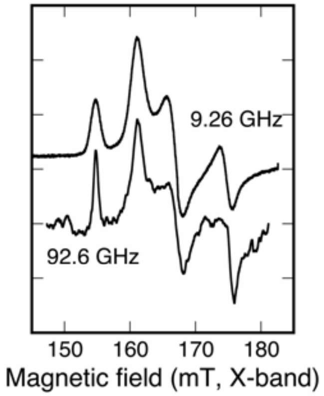

Figure 15. EPR spectra of the high-spin Fe–NO complex of soybean LOX-1 at two frequencies. The soybean lipoxygenase (LOX-1)–nitric oxide complex (3.2 mM in 0.1 M potassium phosphate, pH 7.0) was sealed under argon in a quartz EPR tube of 0.7 mm ID. Spectra were recorded 9.26 GHz and 94 GHz, and the temperature was 6 K. The original 94 GHz spectrum was scaled to the same *g*-value scale as the 9.26 GHz spectrum, and the magnetic field units are shown for the X-band spectrum. Because of the scaling, the high-frequency spectrum is labeled in the figure as if it was recorded at 92.6 GHz, and the corresponding magnetic field scale would be ten times that shown.

3.2.1. Model Compounds

The similarities and differences between iron–NO and iron–oxygen bonding have been the subjects of debate, and model compounds provide important correlations between structure, spectroscopy, and redox chemistry of iron nitrosyls. The nitrosyl groups in these complexes can be described as NO^+ ($S = 0$), $NO^\bullet$ ($S = 1/2$), NO^- ($S = 0$), NO^- ($S = 1$), and NO^{2-} ($S = 1/2$). The associated iron ions have charges and spins such that the overall numbers of iron d electrons plus NO π^* electrons are 6–8 in most experimentally accessible model compounds. The notation for these complexes follows the Enemark and Feltham conventions [51]. The EPR visible complexes are d^7, or $(Fe–NO)^7$, and d^9, or $(Fe–(NO)_2)^9$. Both $S = 3/2$ and $S = 1/2$ d^7 complexes are found. Table 2 summarizes possible electronic states that might be considered for $d^{6–8}$ iron–nitrosyl complexes. Representative references to those electronic states that are experimentally observed, or calculated, are given in the table footnotes.

Although $S = 1/2$ nitrosyl complexes with heme iron are well known and described, low-spin ($S = 1/2$) non-heme iron–NO examples are uncommon. Debate on the electronic descriptions of the low-spin $d^{6–8}$ series has focused on whether the redox chemistry is ligand centered, as suggested by variation in infrared NO stretching frequencies, or metal centered, as implied by Mössbauer isomer shifts. What Serres et al. [52] describe as "a unified picture of the electronic structure of low-spin non-heme iron nitrosyls in perhaps unprecedented detail" has recently been achieved by combined spectroscopy and density functional theory (DFT) calculations. Iron in this d$^{6–8}$ series was in complex with the pentadentate [Fe(II)NO(cyclam-Ac)] (cyclam = 1,4,8,11-tetraazacyclotetradecane; Ac = a pendant acetyl). Oxidation and reduction were achieved by both electrochemical and chemical redox reactions. The d^7 oxidation state is EPR active, as expected, and is low spin. Experimental and simulated spectra from this work are shown in Figure 16. Two components, a- (70%) and b- (30%), were required to fit the EPR data. Also, linewidths with frequency and *g*-variation were assigned to yield fits over a decade of frequencies. Solvation effects on EPR of the experimental sample present some difficulties, but overall, density functional calculations gave EPR parameters in reasonable agreement with experiment (Table 3). At 34 GHz, resolved nitrogen hyperfine of ~74 MHz is clearly seen associated with the middle *g*-value in the spectrum of the minor component. This experimental hyperfine value agrees well with a B3LYP calculation that gives a deviation of 21° between axes of middle *g*-value and maximum hyperfine (86 MHz), giving a calculated value of cos (21°) × 86 MHz ~ 80 MHz. From combined spectroscopy and calculation, the low-spin d^7 complex is best described as (Fe(II) (S = 0) (NO•) (S = 1/2))^7. The (Fe–NO)^8 component, described as "elusive," was partially characterized by experiment and fully by calculation in this same paper. In summary, calculations and spectroscopy lead to a picture of oxidation/reduction in the low-spin d$^{6–8}$ series as ligand centered, with iron remaining Fe(II) through the series.

Table 2. Possible Electronic States and Total Spin (S_{tot}) of (Fe–NO)$^{6–8}$ Complexes[a]

(Fe–NO)^6 $S_{\text{tot}} = 0$	(Fe–NO)^7 $S_{\text{tot}} = ½$	(Fe–NO)^7 $S_{\text{tot}} = 3/2$	(Fe–NO)^8 $S_{\text{tot}} = 0$	(Fe–(NO)$_2$)^9 $S_{\text{tot}} = 1/2$
[Fe(II)NO$^+$] $S = 0, S = 0$[b,d]	[Fe(II)NO$^{\bullet}$] $S = 0, S = 1/2$[b,e]	[Fe(II)NO•] $S = 2, S = 1/2$	[Fe(II)NO$^-$] $S = 0, S = 0$[b]	Nonequivalent NOs
[Fe(III)NO•] $S = 1/2, S = 1/2$[f]	[Fe(III)NO$^-$] $S = 1/2, S = 0$	[Fe(III)NO$^-$] $S = 5/2, S = 1$[c]	[Fe(III)NO^{2-}] $S = 1/2, S = 1/2$	
[Fe(IV)NO$^-$] $S = 1, S = 1$[g]	[Fe(III)NO$^-$] $S = 1/2, S = 1$			

[a] Table modeled, in part, after Chart 1 in Serres et al. [52]. Representative references to states assigned in model compounds are designated in footnotes b–g. [b] [52]. [c] [53,54]. [d] [66]. [e] Typical of heme Fe(II)NO. See D. Singel, Chapter 9, this volume. [f] [61]. [g] [31].

Several model iron–nitrosyl compounds with S = 3/2 group spins were examined by optical, infrared, resonance Raman, x-ray absorption, and calculations [53]. The data indicate a description of the complexes as antiferromagnetically coupled (Fe(III) (S = 5/2) (NO$^-$) (S = 1))^7. A number of other studies of model compounds agree with this assignment of S_{tot} = 3/2 Fe–NO model compounds. In a separate study, the *cis*- and *trans*- isomers of the iron complex of 1,4,8,11-tetraazacyclotetradecane (cyclam), [(cyclam)Fe(II)(NO)(I)], were examined by Mössbauer [54]. The *trans*-cyclam derivative exhibits $S = 1/2$, whereas the *cis*-compound is $S = 3/2$. The *cis*-complex rapidly converts to *trans*- on slight warming of a freeze-trapped sample of the *cis*-cyclam.

Table 3. EPR Parameters from Experiment and DFT Calculation for $S = 1/2$ d^7 Model[a]

EPR parameter	Experimental[b]	Calculated[c]
g_x, g_y, g_z	2.042, 2.022, 1.977	2.017, 1.997, 1.940
A_x, A_y, A_z (MHz)	30, 75, 3	52.9, 86.2, 11.4

[a] From Serres et al. (52), Tables 3 and 10.
[b] Of the two components, the major, a (70%), with more poorly resolved ^{14}N (of NO) hyperfine, is cited.
[c] B3LYP DFT calculation.

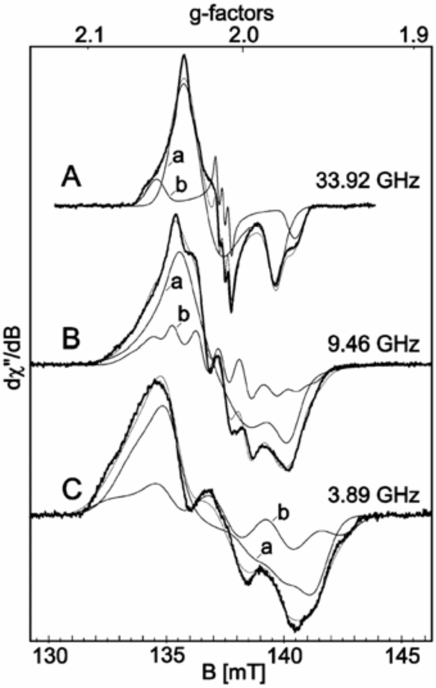

Figure 16. EPR spectra at three frequencies of low-spin model Fe—NO compounds. The EPR spectra of a frozen solution (in butyronitrile) of 1,4,8,11-tetraazacyclotetradecane-1-acetic acid nitrosyl(iron) (PF6) was measured at low temperature (40 K, 33.9202 GHz; 10 K, 9.4565 GHz; 13K, 3.8835 GHz). The *g*-values are given in the labels for the upper abscissa. The lower abscissa is labeled with the corresponding magnetic field for the 3.8835 GHz EPR spectrum. Two forms, in a ratio of 70:30, were used in a simulation (thin lines). The figure is reproduced from Fig. 9 of Serres et al. [52], with permission of the publisher.

3.2.2. *Fe–NO as a Model of Iron-Reactive Oxygen Intermediates in Proteins*

Nitric oxide reacts with non-heme, mononuclear iron in proteins that have diverse interactions with reactive oxygen. The way in which Fe–NO serves as a model of the interaction therefore varies. The ferrous form of facial triad oxygenases [4] reacts with oxygen, forming initially a ferric superoxide intermediate followed by O–O bond cleavage to give the reactive species Fe(IV)–OH. When NO is substituted for oxygen, the analog of the superoxide intermediate is formed as a stable species:

$$\mathrm{Fe(II)(NO)} \leftrightarrow \mathrm{Fe(III)\text{-}NO^-}\ \text{ stable analog of }\ \mathrm{Fe(II)(OO)} \leftrightarrow \mathrm{Fe(III)\text{–}OO^-}.$$

In contrast, superoxide reacts with ferrous iron in SOR, and in this case, the ferrous–NO ↔ ferric–NO$^-$ interaction must model formation of a ferric–peroxyl complex, but with one less electron [55]:

$$\mathrm{Fe(II)\text{–}OO^-} \leftrightarrow \mathrm{Fe(III)\text{–}OO^{2-}}.$$

In the third example, no evidence has been obtained, despite serious effort [56], for direct interaction of oxygen with the ferrous iron in lipoxygenase, but NO forms a complex with a pH-dependent K_d in the range 10–95 μM [49]. Instead, the lipoxygenase iron–NO complex (Figure 15) could be viewed as a model of an intermediate in the catalytic cycle:

$$\mathrm{R\text{-}OO\bullet + Fe(II)} \leftrightarrow \mathrm{ROO^- + Fe(III)}.$$

Regardless of the details of the model, the various stable complexes of ferrous iron with NO prepare non-heme mononuclear iron proteins for high-resolution local structure EPR studies, especially by ENDOR.

3.3. High-Spin NO Complexes with Non-Heme Iron Proteins

3.3.1. *ENDOR Studies of Ligand Rearrangement in Facial Triad Oxygenase-NO Complexes*

A function of the iron center in the "facial triad" oxygenases is to bring three exogenous ligands into alignment for reaction while also remaining tightly attached to three protein sidechains. Nitric oxide serves as a noncleaved oxygen surrogate in structural studies of substrate/inhibitor binding to these oxygenases. Questions regarding rearrangements of exogenous ligand sites have arisen in comparisons of x-ray structures of various facial triad oxygenases in different intermediate states [57]. Magnetic resonance of the solution state provides a versatile companion to the structural studies.

High-resolution ENDOR of iron–NO complexes has proven ideal for resolving questions about the relative orientations of exogenous iron ligands in facial triad oxygenases. Because this volume has a chapter devoted to recent ENDOR studies (see Chapter 3), only a brief account of one example, in which an Fe–NO complex is examined by ENDOR, will be given here. The enzyme 1-aminocyclopropane-1-carboxylic acid oxidase (ACCO) is a facial triad oxygenase involved in ethylene formation. The high resolution achieved in ENDOR studies of ACCO included higher-frequency (35 GHz) pulsed techniques and genetic manipulations designed to facilitate selective isotope labeling [44,58]. The protein-derived metal ligands of ACCO are provided by two His and a carboxylate, bound in bidentate fashion. Nitric oxide reacts with ferrous ACCO to form a high-spin d^7 ($S = 3/2$) complex exhibiting an EPR spectrum indicative of near axial symmetry ($g_{1,2,3}$ = 4.11, 3.94, 1.99; E/D = 0.008). With substrate or inhibitor present, the EPR spectrum is less axial ($g_{1,2,3}$ = 4.23, 3.82, 1.99; E/D = 0.035) [44]. Besides the change in rhombicity, another indication of considerable differences in the electronic structure of the Fe–NO centers between ACCO–NO and the ACCO–NO–substrate complex (ACCO–ACC–NO) is that the latter saturates at ~10-fold lower power than the former.

The problem posed by earlier crystallography studies of other facial triad oxygenases [57] is that the carboxylate of the bidentate substrate and a water ligand are bound to iron in different arrangements in crystal structures of different members of the facial triad oxygenase family. A variety of approaches have now resolved the structural questions by showing that the arrangement of ligands can change when both NO (or, by analogy, oxygen) and substrate bind. The ENDOR studies [44] of ACCO–NO–substrate illustrate this point nicely. All of the protein and ligand nuclei coordinated to iron, except the substrate –COOH oxygen, were labeled with ^{14}N, ^{15}N, or ^{17}O in this study. Overall, combined pulsed and CW ENDOR techniques yielded spectra from both ν_+ and ν_- branches and a full range of g-values. In CW mode, only the ν_+ branch is seen, simplifying the spectra. CW ENDOR was also best in providing information near $g = 2$ (g_3) and at angles intermediate between the extreme g-values in angle-selected experiments. Davies-pulsed 35-GHz ENDOR spectra were better resolved than CW ENDOR spectra around g_1 and g_2. The presence of an iron–water bond in ACCO–NO (no substrate) was detected in two ways. CW ENDOR at g_3 of the enzyme prepared in H_2O^{17} gave a very large ^{17}O resonance at 13 MHz. Also, a 35-GHz refocused-Mims-pulsed ENDOR experiment detected a 2-MHz splitting for the deuterons of D_2O. Whether one or two waters contributed to the data could not be determined. In nitrogen ENDOR of substrate-free ACCO–NO, the two nitrogen nuclei of histidines coordinated to Fe are magnetically identical along g_3 (the Fe–N_{NO} bond direction) and must, therefore, lie in the plane perpendicular to the Fe–N_{NO} direction. In the ACCO–NO–ACC complex, however, they are distinct, one being aligned with g_3 and the other with g_2. Figure 17 shows the angle-selected, 35-GHz CW ENDOR results for the (^{15}N-His)–ACCO–NO–ACC complex. Note that, in the lowest spectrum, taken along g_3, the two ^{15}N–His signals are distinctly different. This finding signifies that one of the Fe–N_{His} bonds has become *trans* to the Fe–N_{NO} direction. If NO is viewed as a paramagnetic oxygen surrogate, then the ENDOR results show that the orientation of oxygen is directed to a unique ligand position on iron, the correct position for subsequent reaction, by the substrate displacing waters and binding in a bidentate fashion [44].

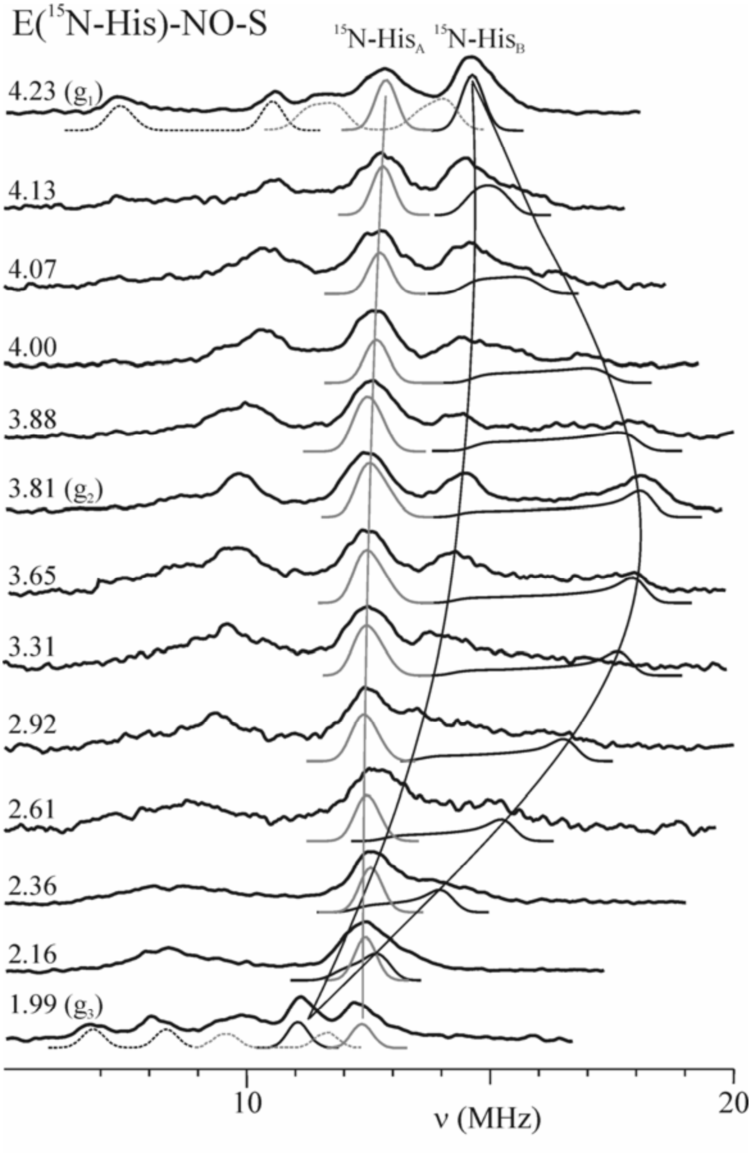

Figure 17. Orientation-selected CW ENDOR spectra (^{15}N–His at 35 GHz) of the enzyme, 1-aminocyclopropane-1-carboxylic acid oxidase (ACCO). At each *g*-value, the upper spectrum is experimental, and below each a simulation is shown. Simulations of individual ^{15}N–His spectra are shown as gray and black for His$_A$ and His$_B$, respectively. The simulation at g_1 ($g = 4.23$) also includes ^{14}NO (long dashes). Note that the two nitrogens of histidine ligands are not equivalent along g_3 (the Fe–N$_{NO}$ bond direction), so one of the histidines is *trans* to the NO ligand. The apparent absence of angle dependence of the ^{15}N–His$_A$ spectra arises from compensating shifts in $\nu_N(^{15}N)$ and nitrogen hyperfine coupling. The figure is reproduced from Fig. 6 of Tierney et al. [44], with permission of the publisher.

3.3.2. Proteins in which NO Is a Natural Ligand to Mononuclear Non-Heme Iron

3.3.2.1. NO responsive transcription factor NorR. E. coli genes for proteins involved in reduction of nitric oxide are transcribed in response to NorR. Transcriptional activation controlled by NorR involves three domains in the protein. An N-terminal GAF domain is the sensor, a middle domain is in the AAA+ family of adenosine triphosphatases (ATPases), and the C-terminal domain is a helix–loop–helix deoxyribonucleic acid (DNA) binding domain. The AAA+ domain is only active when NO has bound to the GAF domain [59]. The GAF domain contains iron and undergoes a conformational change when NO binds iron. In the NO-bound state, NorR then activates transcription. Mutation of one of the iron ligands, D99A, gives a GAF domain that does not bind Fe. The EPR spectrum of NorR–Fe–NO is typical of a d^7 $S = 3/2$ species ($E/D = 0.03$) [47].

3.3.2.2. Nitrile hydratase. Nitric oxide is a naturally occurring ligand in inactive Fe nitrile hydratase, as isolated. This state is EPR silent. In addition to the natural NO ligand, the iron ligand environment is unique in other ways. Three ligands derive from cysteine, but in the highest-resolution x-ray structure two of the sulfur ligands are oxidized sulfurs, sulfinic and sulfonic acids, and the third sulfur is cysteinate [60]. Photolysis of the NO ligand from nitrile hydratase replaces NO by water and yields an enzymatically active state with a low-spin ferric EPR signal [31]. On the basis of several forms of spectroscopy, the Fe(III)–NO form of nitrile hydratase is assigned as low-spin Fe(III)NO, d^6. This interesting iron center is the subject of ongoing modeling and theory, showing that the charge density on iron in the NO-bound d^6 form is similar to that in the photolysed FeIII form [61]. The center is therefore closer to [Fe(III)NO$^\bullet$], [$S = 1/2$, $S = 1/2$], than to other charge and spin designations (Table 2).

3.4. Low-Spin NO Complexes with Non-Heme Iron Proteins

3.4.1. d^7 Example: Protocatechuate 3,4-Dioxygenase

Under most conditions, ferrous protocatechuate 3,4-dioxygenase (3,4-PCD) gives EPR spectra of a high-spin, $S = 3/2$, nitrosyl adduct, but when NO is added to a preformed 3,4-PCD–cyanide complex, a well-resolved EPR spectrum of a low-spin adduct (d^7, $S = 1/2$) is seen [62]. A calculation using the published parameters of this low-spin ^{15}NO adduct is illustrated in Figure 18. In variously isotope-labeled samples, the signals have resolved splittings from ^{15,14}NO, a histidine ^{14}N, and ^{13}C–cyanide ligands with resolution as high as many previously reported for NO associated with iron in heme proteins. Binding of both cyanide and NO depends on the order of addition. When CN$^-$ binds first, a tyrosine ligand is probably displaced, maintaining charge neutrality, and subsequently NO and one more CN$^-$ bind. The Fe–NO bond is photolabile. Assignment of the EPR spectra helped establish how the conformation of the iron center adapts to exogenous ligands. The highly resolved hyperfine splittings indicate close alignment of the principal axes of the **g**- and **A**-tensors.

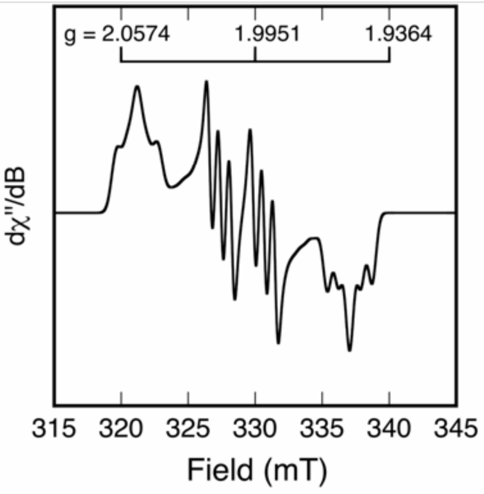

Figure 18. A simulation, after that of Orville and Lipscomb [62], of the EPR spectrum of 3,4-protocatechuate dioxygenase with cyanide and ^{15}N-nitric oxide. The original appears in Fig. 3B of Orville and Lipscomb [62]. The simulation here was performed with XSophe [37] with g_1 = 2.050, g_2 = 2.001, g_3 = 1.9535; ^{15}N-NO A_1 = 41.9, A_2 = 91, A_3 = 45 MHz; ^{14}N-protein A = 2.3 MHz (isotropic); linewidths at $g_{1,2,3}$ = 0.425, 0.225, and 0.35 mT; microwave frequency = 9.2158 GHz; 40 field partitions; and 32 grid segments. It is interesting to compare this spectrum to those of a model d^7, S = 1/2 compound shown in Figure 16.

3.4.2. d^9 Example: When Spin Counts Matter: Fur-$(NO)_2$

Fur, the iron uptake regulator of Gram-negative bacteria, binds to "iron boxes" and is a corepressor for genes involved in iron homeostasis and oxygen stress [46]. FeFur includes six iron donor ligands (oxygen plus nitrogen), and the mechanism of Fur regulation involves association–dissociation of the iron–protein complex. The *E. coli* FeFur repressor activity is inhibited by NO, concomitant with formation of a complex having an EPR spectrum with g_{iso} = 2.03 [48]. This nitric–oxide interaction links bacterial NO stress responses to iron homeostasis. The protein has a second metal ion center, a zinc site in an $(S_2(O/N)_2)$ environment, and it also has two free sulfhydryls that are not involved in either metal center (shown by mutagenesis). When NO binds to FeFur, the resulting EPR spectrum is identical to the well-known d^9 iron-dinitrosyl species formed when NO reacts with iron sulfur centers. This result is illustrated in Figure 19, where the d^9 iron dinitrosyl species resulting from an iron–sulfur protein [63] is compared to a simulation using the EPR parameters that fit the FeFur spectrum [48].

A remaining question is whether the new d^9 iron-nitrosyl center might involve a rearrangement to include the sulfurs of the zinc center. The extremely tight binding of zinc to the second metal site in Fur suggests not, but accounting quantitatively for the number of nitric oxides involved in forming NO–FeFur has been important. Fur has higher affinity for NO than deoxymyoglobin has, and the equivalents of NO needed to saturate FeFur could therefore be determined optically in the presence of deoxymyoglobin (see supporting information in [48]). The answer obtained was that 2.7 equivalents of NO were needed to saturate the FeFur site. The extra NO equivalent served as a reductant to give the paramagnetic d^9 complex. The conclusion then is that FeFur forms predominantly (85%) a protein–$(Fe(NO)_2)^9$ ($S = 1/2$) complex and a minor amount of an EPR-silent $(Fe(NO)_2)^8$ ($S = 0$) complex (assigned by Mössbauer). In contrast to d^7 Fe–NO EPR spectra, the d^9 species in FeFur has a small nitrogen hyperfine (around 10 MHz or less) and a large ^{57}Fe hyperfine, showing that the spin density is high on iron and low on NO.

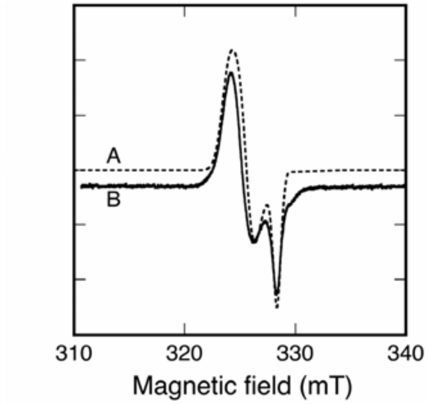

Figure 19. The calculated EPR spectrum of the d^9, $S = 1/2$, FeFur$(NO)_2$ complex compared with the experimental iron dinitrosyl complex from an iron–sulfur protein, RumA. The upper spectrum (dashed line) is a simulation (XSophe [37]) based on the parameters given by D'Autréaux et al. [48] (their Fig. 3 legend] for the EPR of an FeFur complex with two ^{14}N–NO molecules. Simulation parameters used here were spin state, S = 1/2; $g_{1,2,3}$-values, 2.042, 2.032, 2.015; linewidths at each g-value, 7.9, 7.0, 4.0. The ^{14}N–NO hyperfine was not used in the simulation shown, but incorporating hyperfine splitting from ^{14}N of up to 10, 10, and 5 MHz (*x, y, z*) produced no significant change in the calculated lineshape. The lower curve is an experimental spectrum that results from NO addition to the $[Fe_4S_4]^{2+}$ cluster in the *E. coli* RNA methylase, RumA. The frequency used in simulation was 9.26 GHz, to match the RumA EPR spectrum. The experimental spectrum was published earlier as Fig. 5b of Agarwalla et al. [63].

The x-ray structure of Fur from *Pseudomonas aeruginosa*, solved recently [64], is the first structure of a Fur protein. In this organism the protein has only one sulfhydryl, and it lacks the domain with the high-affinity zinc site of the *E. coli* homolog. Still, it was found to have two metal sites, one (O_4/N_2) octahedral site for iron and one tetrahedral (O_2/N_2) site occupied by zinc. All the metal-binding amino acids are conserved in the *P. aeruginosa* and *E. coli* homologs, so an unidentified metal (M) in a tetrahedral site in Fur proteins, such as the one from *E. coli*, might yield a dinitrosyl complex with geometry similar to those formed in Fe–S proteins. However, more recent examination of metal affinities of *E. coli* Fur cast doubt on the existence of the putative tetrahedral site in this version of the protein [65]. Evidently the story of Fur EPR is not over.

REFERENCES

1. Gaffney BJ, Silverstone HJ. 1993. Simulation of the EMR spectra of high-spin iron in proteins. In *EMR of paramagnetic molecules*, pp. 1–57. Ed LJ Berliner, J Reuben. *Biological magnetic resonance*, Vol. 13. New York & London: Plenum Press.
2. Abu-Omar MM, Loaiza A, Hontzeas N. 2005. Reaction mechanisms of mononuclear non-heme iron oxygenases. *Chem Rev* **105**(6):2227–2252.
3. Costas M, Mehn MP, Jensen MP, Que L. 2004. Dioxygen activation at mononuclear nonheme iron active sites: enzymes, models, and intermediates. *Chem Rev* **104**(2):939–986.
4. Hausinger RP. 2004. FeII/alpha-ketoglutarate-dependent hydroxylases and related enzymes. *Crit Rev Biochem Mol Biol* **39**(1):21–68.
5. Solomon EI, Brunold TC, Davis MI, Kemsley JN, Lee SK, Lehnert N, Neese F, Skulan AJ, Yang YS, Zhou J. 2000. Geometric and electronic structure/function correlations in non-heme iron enzymes. *Chem Rev* **100**(1):235–349.
6. Kappock TJ, Caradonna JP. 1996. Pterin-dependent amino acid hydroxylases. *Chem Rev* **96**(7):2659–2756.
7. Kurtz DM. 2004. Microbial detoxification of superoxide: the non-heme iron reductive paradigm for combating oxidative stress. *Acc Chem Res* **37**(11):902–908.
8. Clay MD, Jenney FE, Hagedoorn PL, Goerge GN, Adams MWW, Johnson MK. 2002. Spectroscopic studies of *Pyrococcus furiosus* superoxide reductase: implications for active-site structures and the catalytic mechanism. *J Am Chem Soc* **124**(5):788–805.
9. Dubach J, Gaffney BJ, More K, Eaton GR, Eaton SS. 1991. Effect of the synergistic anion on electron paramagnetic resonance spectra of iron–transferrin anion complexes is consistent with bidentate binding of the anion. *Biophys J* **59**(5):1091–1100.
10. Yeh AP, Hu YL, Jenney FE, Adams MWW, Rees DC. 2000. Structures of the superoxide reductase from *Pyrococcus furiosus* in the oxidized and reduced states. *Biochemistry* **39**(10):2499–2508.
11. Baker HM, Anderson BF, Brodie AM, Shongwe MS, Smith CA, Baker EN. 1996. Anion binding by transferrins: importance of second-shell effects revealed by the crystal structure of oxalate-substituted diferric lactoferrin. *Biochemistry* **35**(28):9007–9013.
12. Bloom LM, Benkovic SJ, Gaffney BJ. 1986. Characterization of phenylalanine hydroxylase. *Biochemistry* **25**(15):4204–4210.
13. Yang AS, Gaffney BJ. 1987. Determination of relative spin concentration in some high-spin ferric proteins using E/D-distribution in electron paramagnetic resonance simulations. *Biophys J* **51**(1):55–67.
14. Gaffney BJ, Mavrophilipos DV, Doctor KS. 1993. Access of ligands to the ferric center in lipoxygenase-1. *Biophys J* **64**(3):773–783.
15. Gaffney BJ, Su C, Oliw EH. 2001. Assignment of EPR transitions in a manganese-containing lipoxygenase and prediction of local structure. *Appl Magn Reson* **21**(3–4):411–422.

16. Bennati M, Prisner TF. 2005. New developments in high field electron paramagnetic resonance with applications in structural biology. *Rep Prog Phys* **68**(2):411–448.
17. Andersson KK, Schmidt PP, Katterle B, Strand KR, Palmer AE, Lee SK, Solomon EI, Graslund A., Barra AL. 2003. Examples of high-frequency EPR studies in bioinorganic chemistry. *J Biol Inorg Chem* **8**(3):235–247.
18. Gaffney BJ, Maguire BC, Weber RT, Maresch GG. 1999. Disorder at metal sites in proteins: a high-frequency-EMR study. *Appl Magn Reson* **16**(2):207–221.
19. Aasa R, Vänngård T. 1975. EPR signal intensity and powder shapes: a reexamination. *J Magn Reson* **19**(3):308–315.
20. Pilbrow JR, Sinclair GR, Hutton DR, Troup GJ. 1983. Asymmetric lines in field-swept EPR:Cr^{3+} looping transitions in ruby. *J Magn Reson* **52**(3):386–399.
21. Gaffney BJ, Silverstone HJ. 1998. Simulation methods for looping transitions. *J Magn Reson* **134**(1):57–66.
22. Fiamingo FG, Brill AS, Hampton DA, Thorkildsen R. 1989. Energy distributions at the high-spin ferric sites in myoglobin crystals. *Biophys J* **55**(1):67–77.
23. Rakowsky MH, Zecevic A, Eaton GR, Eaton SS. 1998. Determination of high-spin iron(III)-nitroxyl distances in spin-labeled porphyrins by time-domain EPR. *J Magn Reson* **131**(1):97–110.
24. Berliner LJ, Eaton GR, Eaton SS, eds. 2000. *Distance measurements in biological systems by EPR. Biological magnetic resonance*, Vol. 19. New York: Kluwer Academic/Plenum.
25. MacArthur R, Sazinsky MH, Kuhne H, Whittington DA, Lippard SJ, Brudvig GW. 2002. Component B binding to the soluble methane monooxygenase hydroxylase by saturation-recovery EPR spectroscopy of spin-labeled MMOB. *J Am Chem Soc* **124**(45):13392–13393.
26. Bennati M, Robblee JH, Mugnaini V, Stubbe J, Freed JH, Borbat P. 2005. EPR distance measurements support a model for long-range radical initiation in *E. coli* ribonucleotide reductase. *J Am Chem Soc* **127**(43):15014–15015.
27. Klug CS, Eaton SS, Eaton GR, Feix JB. 1998. Ligand-induced conformational change in the ferric enterobactin receptor FepA as studied by site-directed spin labeling and time-domain ESR. *Biochemistry* **37**(25):9016–9023.
28. Gaffney BJ, Eaton GR, Eaton SS. 1998. Electron spin relaxation rates for high-spin Fe(III) in iron transferrin carbonate and iron transferrin oxalate. *J Phys Chem B* **102**(28):5536–5541.
29. Hendrich MP, Debrunner PG. 1989. Integer-spin electron paramagnetic resonance of iron proteins. *Biophys J* **56**(3):489–506.
30. Wang DM, Pilbrow JR. 1988. Symmetry relationships for the 4 energy levels and the angular property of the EPR spectra for a spin-3/2 system. *J Magn Reson* **77**(3):411–423.
31. Popescu VC, Munck E, Fox BG, Sanakis Y, Cummings JG, Turner IM, Nelson MJ. 2001. Mössbauer and EPR studies of the photoactivation of nitrile hydratase. *Biochemistry* **40**(27):7984–7991.
32. Fufezan C, Zhang CX, Krieger-Liszkay A, Rutherford AW. 2005. Secondary quinone in photosystem II of *Thermosynechococcus elongatus*: semiquinone-iron EPR signals and temperature dependence of electron transfer. *Biochemistry* **44**(38):12780–12789.
33. Utschig LM, Thurnauner MC, Tiede DM, Poluektov OG. 2005. Low-temperature interquinone electron transfer in photosynthetic reaction centers from *Rhodobacter sphaeroides* and *Blastochloris viridis*: characterization of Q(B)(–) states by high-

frequency electron paramagnetic resonance (EPR) and electron-nuclear double resonance (ENDOR). *Biochemistry* **44**(43):14131–14142.

34. Lakshmi KV, Brudvig GW. 2000. Electron paramagnetic resonance distance measurements in photosynthetic reaction centers. In *Distance measurements in biological systems by EPR*, pp. 513–567. Ed LJ Berliner, GR Eaton, SS Eaton. New York: Kluwer Academic/Plenum.
35. Feher G. 2002. My road to biophysics: picking flowers on the way to photosynthesis. *Annu Rev Biophys Biomol Struct* **31**:1–44.
36. Calvo R, Abresch EC, Bittl R, Feher G, Hofbauer W, Isaacson RA, Lubitz W, Okamura MY, Paddock ML. 2000. EPR study of the molecular and electronic structure of the semiquinone biradical $Q_A^{-\cdot}Q_B^{-\cdot}$ in photosynthetic reaction centers from *Rhodobacter sphaeroides*. *J Am Chem Soc* **122**(30):7327–7341.
37. Hanson GR, Gates KE, Noble CJ, Griffin M, Mitchell A, Benson S. 2004. XSophe-Sophe-XeprView: a computer simulation software suite (v. 1.1.3) for the analysis of continuous wave EPR spectra. *J Inorg Biochem* **98**(5):903–916.
38. Butler WF, Johnston DC, Shore HB, Fredkin DR, Okamura MY, Feher G. 1980. The electronic structure of Fe^{2+} in reaction centers from *Rhodopseudomonas sphaeroides*, I: static magnetization measurements. *Biophys J* **32**(3):967–992.
39. Butler WF, Calvo R, Fredkin DR, Isaacson RA, Okamura MY, Feher G. 1984. The electronic structure of Fe^{2+} in reaction centers from *Rhodopseudomonas sphaeroides*, III: EPR measurements of the reduced acceptor complex. *Biophys J* **45**(5):947–973.
40. Xu Q, Baciou L, Sebban P, Gunner MR. 2002. Exploring the energy landscape for Q_A^- to Q_B electron transfer in bacterial photosynthetic reaction centers: effect of substrate position and tail length on the conformational gating step. *Biochemistry* **41**(31):10021–10025.
41. Calvo, R, Isaacson, RA, Abresch, EC, Okamura, MY and Feher, G. 2002. Spin-lattice relaxation of coupled metal-radical spin dimers in proteins: application to Fe^{2+}-cofactor ($Q_A^{-\bullet}$, $Q_B^{-\bullet}$, $\phi^{-\bullet}$) dimers in reaction centers from photosynthetic bacteria. *Biophys J* **83**(5):2440–2456.
42. Hori H, Ikeda-Saito M, Yonetani M. 1981. Single crystal EPR of myoglobin nitroxide: freezing-induced reversible changes in the molecular orientation of the ligand. *J Biol Chem* **256**(15):7849–7855.
43. Galpin JR, Veldink GA, Vliegenthart JFG, Boldingh J. 1978. The interaction of nitric oxide with soybean lipoxygenase-1. *Biochim Biophys Acta* **536**(2):356–362.
44. Tierney DL, Rocklin AM, Lipscomb JD, Que L, Hoffman BM. 2005. ENDOR studies of the ligation and structure of the non-heme iron site in ACC oxidase. *J Am Chem Soc* **127**(19):7005–7013.
45. Cao M, Moore CM, Helmann JD. 2005. *Bacillus subtilis* paraquat resistance is directed by σ_M, an extracytoplasmic function sigma factor, and is conferred by YqjL and BcrC. *J Bacteriol* **187**(9):2948–2956.
46. Mukhopadhyay P, Zheng M, Bedzyk LA, LaRossa RA, Storz G. 2004. Prominent roles of the NorR and Fur regulators in the *Escherichia coli* transcriptional response to reactive nitrogen species. *Proc Natl Acad Sci USA* **101**(3):745–750.
47. D'Autreaux B, Tucker NP, Dixon R, Spiro S. 2005. A non-haem iron centre in the transcription factor NorR senses nitric oxide. *Nature* **437**(7059):769–772.
48. D'Autreaux B, Horner O, Oddou JL, Jeandey C, Gambarelli S, Berthomieu C, Latour JM, Michaud-Soret I. 2004. Spectroscopic description of the two nitrosyl-iron complexes responsible for fur inhibition by nitric oxide. *J Am Chem Soc* **126**(19):6005–6016.

49. Nelson MJ. 1987. The nitric oxide complex of ferrous soybean lipoxygenase-1: substrate, pH, and ethanol effects on the active-site iron. *J Biol Chem* **262**(25):12137–12142.

50. Schenk G, Neidig ML, Zhou J, Holman TR, Solomon EI. 2003. Spectroscopic characterization of soybean lipoxygenase-1 mutants: the role of second coordination sphere residues in the regulation of enzyme activity. *Biochemistry* **42**(24):7294–7302.

51. Enemark JH, Feltham RD. 1974. Principles of structure, bonding, and reactivity for metal nitrosyl complexes. *Coord Chem Rev* **13**(9):339–406.

52. Serres RG, Grapperhaus CA, Bothe E, Bill E, Weyhermuller T, Neese F, Wieghardt K. 2004. Structural, spectroscopic, and computational study of an octahedral, non-heme $[\text{Fe–NO}]^{(6–8)}$ Series: $[\text{Fe(NO)(cyclam-ac)}]^{2+/+/0}$. *J Am Chem Soc* **126**(16):5138–5153.

53. Brown CA, Pavlosky MA, Westre TE, Zhang Y, Hedman B, Hodgson KO, Solomon EI. 1995. Spectroscopic and theoretical description of the electronic structure of $S = 3/2$ iron-nitrosyl complexes and their relation to O_2 activation by non-heme iron enzyme active sites. *J Am Chem Soc* **117**(2):715–732.

54. Hauser C, Glaser T, Bill E, Weyermuller T, Wieghardt K. 2000. The electronic structures of an isostructural series of octahedral nitrosyliron complexes {Fe–NO}6,7,8 elucidated by Mössbauer spectroscopy. *J Am Chem Soc* **122**(18):4352–4365.

55. Clay MD, Cosper CA, Jenney FE, Adams NWW, Johnson MK. 2003. Nitric oxide binding at the mononuclear active site of reduced *Pyrococcus furiosus* superoxide reductase. *Proc Natl Acad Sci USA* **100**(7):3796–3801.

56. Knapp MJ, Klinman JP. 2003. Kinetic studies of oxygen reactivity in soybean lipoxygenase-1. *Biochemistry* **42**(39):11466–11475.

57. Zhang ZH, Ren JS, Harlos K, McKinnon CH, Clifton IJ, Schofield CJ. 2002. Crystal structure of a clavaminate synthase–Fe(II)–2-oxoglutarate–substrate–NO complex: evidence for metal centered rearrangements. *FEBS Lett* **517**(1–3):7–12.

58. Rocklin AM, Tierney DL, Kofman V, Brunhuber NMW, Hoffman BM, Christoffersen RE, Reich NO, Lipscomb JD, Que L. 1999. Role of the nonheme Fe(II) center in the biosynthesis of the plant hormone ethylene. *Proc Natl Acad Sci USA* **96**(14):7905–7909.

59. Tucker NP, D'Autreaux B, Studholme DJ, Spiro S, Dixon R. 2004. DNA binding activity of the *Escherichia coli* nitric oxide sensor NorR suggests a conserved target sequence in diverse proteobacteria. *J Bacteriol* **186**(19):6656–6660.

60. Nagashima S, Nakasako M, Dohmae N, Tsujimura M, Takio K, Odaka M, Yohda M, Damiya N, Endo I. 1998. Novel non-heme iron center of nitrile hydratase with a claw setting of oxygen atoms. *Nat Struct Biol* **5**(5):347–351.

61. Dey A, Chow M, Taniguchi K, Lugo-Mas P, Davin S, Maeda M, Kovacs JA, Odaka M, Hodgson KO, Hedman B, Solomon EI. 2006. Sulfur K-edge XAS and DFT calculations on nitrile hydratase: geometric and electronic structure of the non-heme iron active site. *J Am Chem Soc* **128**(2):533–541.

62. Orville AM, Lipscomb JD. 1997. Cyanide and nitric oxide binding to reduced protocatechuate 3,4-dioxygenase: insight into the basis for order-dependent ligand binding by intradiol catecholic dioxygenases. *Biochemistry* **36**(46):14044–14055.

63. Agarwalla S, Stroud RM, Gaffney BJ. 2004. Redox reactions of the iron-sulfur cluster in a ribosomal RNA methyltransferase, RumA: optical and EPR studies. *J Biol Chem* **279**(33):34123–34129.

64. Pohl E, Haller JC, Mijovilovich A, Meyer-Kaucke W, Garman E, Vasil ML. 2003. Architecture of a protein central to iron homeostasis: crystal structure and spectroscopic analysis of the ferric uptake regulator. *Mol Microbiol* **47**(4):903–915.

65. Mills SA, Marletta MA. 2005. Metal binding characteristics and role of iron oxidation in the ferric uptake regulator from *Escherichia coli*. *Biochemistry* **44**(41):13553–13559.
66. Lee CM, Hsieh CH, Dutta A, Lee GH, Liaw WF. 2003. Oxygen binding to sulfur in nitrosylated iron–thiolate complexes: relevance to the Fe-containing nitrile hydratases. *J Am Chem Soc* **125**(38):11492–11493.
67. Erlandsen H, Fusetti F, Martinez A, Hough E, Flatmark T, Stevens, RC. 1997. Crystal structure of the catalytic domain of human phenylalanine hydroxylase reveals the structural basis for phenylketonuria. *Nat Struct Biol* **4**(12):995–1000.
68. Minor W, Steczko J, Stec B, Otwinowski Z, Bolin JT, Walter R, Axelrod B. 1996. Crystal structure of soybean lipoxygenase L-1 at 1.4 Å resolution. *Biochemistry* **35**(33):10687–10701.
69. Shiota Y, Yoshizawa K. 2004. QM/MM study of the mononuclear non-heme iron active site of phenylalanine hydroxylase. *J Phys Chem B* **108**(44):17226–17237.
70. Lehnert N, Solomon EI. 2003. Density-functional investigation on the mechanism of H-atom abstraction by lipoxygenase. *J Biol Inorg Chem* **8**(3):294–305.